Chapter 30 – NUMERICAL SOLUTIONS FOR THE VFE-2 CONFIGURATION ON UNSTRUCTURED GRIDS AT KTH, SWEDEN

by

Simone Crippa

30.1 INTRODUCTION

The flow over a sharp and blunt leading edged, slender delta wing is considered in this chapter under subsonic and transonic conditions. The range of Mach number presented here extends from 0.2 to 0.85 and the range of Reynolds number form 2 to 120 million. This investigation was undertaken as part of the 2nd International Vortex Flow Experiment (VFE-2), a facet of the NATO RTO AVT-113 Task Group, which was set up to consider the flow behaviour both experimentally and computationally over a specified delta wing of 65° sweep.

30.2 MODEL DESCRIPTION

The geometry proposed by Hummel and Redeker [30-16] for the VFE-2 project is that of a delta wing with a 65° leading-edge sweep angle (Λ). The initial wind tunnel campaign on which the facet is based on was performed by Chu and Luckring [30-3] in the National Transonic Facility (NTF), NASA Langley Research Center (LaRC). A remarkable feature of the wind tunnel model is the possibility to interchange the leading-edge section which is attached to the flat-plate central wing section. Three blunt leading-edge radii (r) and a sharp leading edge were originally tested. But for the AVT-113/VFE-2 project, only the sharp ($r/\bar{c} = 0$) and medium radius ($r/\bar{c} = 0.0015$) leading edge geometries were selected for numerical and further experimental evaluations.

30.3 COMPUTATIONAL METHOD

30.3.1 Solver

The flow solver Edge [30-7] is used throughout this study. Edge is an unstructured, edge-based, finite volume CFD code developed and maintained by the Swedish Defence Research Agency (FOI). KTH is one among several academic contributors to the development of the code. Time integration to steady state of the discretised Reynolds averaged Navier-Stokes (RANS) equations is achieved with an explicit three-stage Runge-Kutta scheme. For the spatial discretization, a second order accurate, central scheme with 4th order artificial dissipation set to 0.02 is used for all cases. To speed up convergence, implicit residual smoothing, local time stepping and four level agglomeration multigrid are used.

The turbulence model used for the closure of the RANS equations is the two-equation k-ω model by Hellsten [30-14] coupled to the explicit algebraic Reynolds stress model (EARSM) by Wallin and Johansson [30-30]. A strain-rate based (curvature corrected) modification to EARSM (CC-EARSM) coupled with the Hellsten k-ω model is also evaluated for single cases. The calculations are performed with the assumption of fully turbulent flow, with a free-stream turbulence intensity of 0.1%.

For the unsteady computations, the original Detached Eddy Simulation (DES) [30-27] model as implemented in Edge is used. Time integration is achieved through "dual time stepping", an implicit time marching technique with explicit sub-iterations.

30.3.2 Numerical Model and Boundary Conditions

The geometric description of the configuration is given analytically by Chu and Luckring [30-3]. A half-body, digital geometric definition is available through a Virtual Laboratory [30-20] set up and maintained by NASA LaRC. The origin of the right-handed, Cartesian coordinate system is at the apex of the delta wing with the x-coordinate pointing downstream (towards the sting), the z-coordinate being perpendicular to the flat plate section and the y-coordinate pointing in span-wise direction. The numerical geometry features a root chord (c_r) of 1m resulting in a mean aerodynamic chord ($\bar{c}$) of 2/3 m ≈ 0.667 m, which is hereafter used as reference length for the Reynolds number (R_{mac}). The numerical model for the various grids is the same, apart from the two different leading edge sections. The sting is represented exactly as in the wind tunnel model up to the position $x/c_r = 1.758$, as recommended by Chu and Luckring [30-3]. After this location, the sting is closed out using an elliptical revolution surface, which is continuous through the curvature at cut-off. The total length of the closure surface is five times the diameter of the sting at the cut-off position ($d/c_r = 0.165$), i.e. $x/c_r = 0.826$, see Figure 30-1. The farfield boundary is located at approx. $11 \cdot c_r$ from any wall, in all directions, resulting in a half-sphere farfield boundary with a radius of 12.5 m.

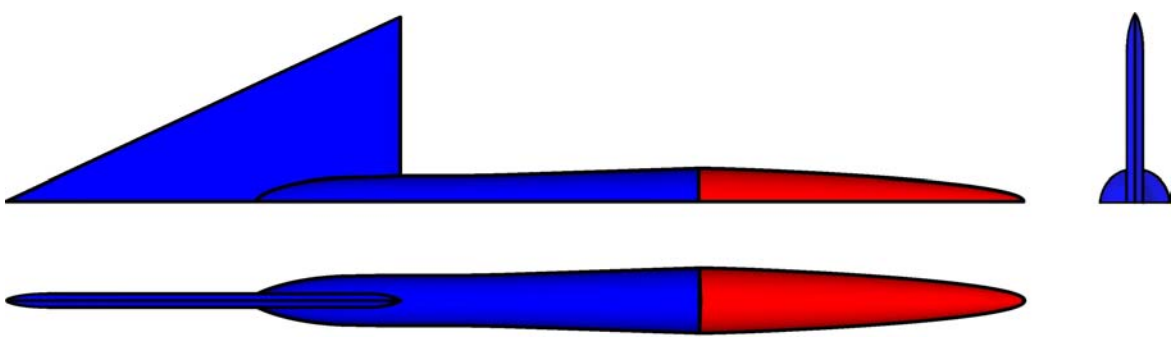

Figure 30-1: Three-View Sketch of Numerical Model – Exact NASA-NTF [30-3] Geometry (in blue) and Sting Close-Off Surface (in red).

A common unstructured grid for the blunt leading-edge geometry is not available, thus for this study it is generated using a combination of the commercially available ANSYS ICEM CFD meshing package and the FOI-internal advancing-front grid generator TRITET [30-28]. The latter is the tool of choice for generating grids for Edge, as it is transparently interfaced to the solution based re-meshing and h-adaptation programs available within the Edge distribution. Although a common unstructured grid is available for the sharp leading edge model, for this work a topologically similar grid as for the blunt leading edge model is used also for the sharp leading edge computations.

Solution based adaptive grid refinement [30-29] is available in Edge and is used extensively throughout this study. Using a flow solution gained on a hybrid grid and a user-defined value for the selected adaptation sensor, the algorithm selects the cell edges to be subdivided and performs cell bisection for tetrahedral and prismatic elements. The prismatic cell elements are subdivided consistently in wall-normal direction to avoid hanging nodes and preserving the prismatic layer structure. This leads to further refinement of surface elements, whereby the additional points are projected to the interpolated location based on the neighbouring

original surface nodes. The algorithm can process only tetrahedral, pyramidal and prismatic volume elements. The available adaptation algorithm features three different vortex-capturing sensors [30-21] based on total pressure ratio, entropy loss or an eigenvalue analysis of the velocity gradient tensor, commonly called λ_2. It is also possible to refine several prismatic layers parallel to the wall for achieving a desired wall-normal non-dimensional cell spacing (y^+).

All grids feature a half-span representation of the delta wing model as described here, with a symmetric boundary condition applied on the symmetry plane. Furthermore, the boundary for the solid walls is of adiabatic, no-slip type for the viscous computations and of slip, wall-bounded type for the inviscid computations. On the farfield boundary a weak formulation characteristic condition is set.

Additional details of the numerical grids for the specific cases are given in the respective section.

30.4 SUBSONIC CASES

The results presented and discussed in this section allow for a deeper and more precise characterization of the unique double vortex system, which develops on the blunt leading edge delta wing at subsonic speeds.

Firstly, computational fluid dynamic (CFD) computations are presented for three Reynolds numbers (2, 6 and 60 million) at two angles of attack (18.5° and 23.0°) for a fixed Mach number of 0.4. Hereby the focus is laid on examining the angle of attack (AOA) dependence of the vortex separation onsets at a given Reynolds number. Secondly, a detailed flow topological analysis at and around the specific case at M = 0.4, α = 13.3°, $R_{mac} = 3 \times 10^6$ is presented. For the flow topological interpretation, solutions at different Mach and Reynolds numbers are employed along with an inviscid case. Comparisons between computational results and experiments are presented with regard to surface pressure coefficient and surface flow patterns for the suction side of the delta wing.

30.4.1 Test Cases

The VFE-2 task group defined a matrix of computational cases based on realistic application problems and CFD development and evaluation needs. Each of the two main geometry configurations (sharp and blunt leading edge) are mainly used to study distinct effects. The conditions for the blunt leading edge geometry were chosen for studying primarily the transition from attached flow to semi-separated vortical flow up to separated dead-water flow. On the other hand, the sharp leading edge conditions were chosen for studying unsteady phenomena such as vortex breakdown and transonic vortex-shock interactions.

For the subsonic computations only the blunt leading edge cases are presented. With the initial case of interest being the M = 0.4, α = 18.5°, $R_{mac} = 6 \times 10^6$ condition. From this condition, a lower and a higher R_{mac} are selected, respectively 2 and 60 million. The $R_{mac} = 6 \times 10^6$ and $R_{mac} = 60 \times 10^6$ wind tunnel data is available from the NTF campaign [30-3]. Unfortunately the $R_{mac} = 2 \times 10^6$ data from the transonic wind tunnel in Göttingen (TWG) of the German-Dutch Wind tunnels (DNW) in Göttingen is not fully published yet, thus the data presented in Konrath et al. [30-17] is used for this comparison. The $R_{mac} = 3 \times 10^6$ runs are available [30-17], [30-18],[30-19]; thus two additional conditions are chosen. One at $R_{mac} = 3 \times 10^6$ for comparison to latest experimental data and another at $R_{mac} = 120 \times 10^6$ to assess the effect of a further increase in Reynolds number.

30.4.1.1 Mid to High Incidence

To evaluate the coupling of angle of attack and Reynolds number, the initial condition are expanded to include also the α = 23.0° conditions. The cases for the AOA-Reynolds number dependency analysis are summarized

in Table 30-1. It is worth to note at this point that the initial VFE-2 test matrix is expanded here by the $R_{mac} = 60 \times 10^6$ cases.

Table 30-1: Test Cases for the AOA-Reynolds Number Dependency Analysis

α	M	R_{mac} $[\cdot 10^6]$
18.5°	0.40	2
18.5°	0.40	6
18.5°	0.40	60
23.0°	0.40	2
23.0°	0.40	6
23.0°	0.40	60

The free-stream conditions from the experimental campaign differ slightly from the VFE-2 computational matrix. The cases used for comparison are listed in Table 30-2.

Table 30-2: Experimental Cases Selected for Comparison (from Chu and Luckring [30-3])

Run number	Point number	α	M	R_{mac} $[\cdot 10^6]$
3	54	18.4°	0.400	6
21	424	18.3°	0.398	59.6
3	56	22.4°	0.400	6
21	426	22.4°	0.398	59.6

30.4.1.2 Low Incidence

At the establishment of the VFE-2 task group, one of the main cases of interest was the $\alpha = 13.3°$, $R_{mac} = 6 \times 10^6$, M = 0.4 condition for the blunt leading-edge configuration. This condition was selected since it exhibits the most distinctive trace of the inner vortex from the complete initial dataset (Chu and Luckring [30-3]). The availability of further, more detailed data from other experimental campaigns is mainly limited to lower Reynolds numbers. To harvest the most from the new experimental data, a shift of the computational efforts to lower Reynolds numbers was necessary. Thus a second set of conditions was chosen to tackle the flow topological description of the dual, co-rotating vortex system. Additionally to the M = 0.4 conditions, a further case is chosen at M = 0.2, $\alpha = 13°$, $R_{mac} = 2 \times 10^6$. Further analysis based on the solution of the Euler equations for the nominal conditions of $\alpha = 13.3°$ and M = 0.4, is helpful to assess the development of the flowfield in the theoretical inviscid assumption. The cases presented for this evaluation are listed in Table 30-3.

Table 30-3: Test Cases for the Flow Topology Study

α	13°	13.3°	13.3°	13.3°	13.3°	13.3°	13.3°
M	0.20	0.40	0.40	0.40	0.40	0.40	0.40
R_{mac} $[\cdot 10^6]$	2	2	3	6	60	120	- (inviscid)

30.4.2 Numerical Grids

Three similar numerical grids are employed within this study. Two hybrid grids consisting of tetrahedral volume elements and prismatic elements for the viscous layer resolution on an isotropic triangle-elements surface grid.

The main difference between the two hybrid grids is the targeted Reynolds number range (low or high) as well as the leading-edge resolution. The first hybrid grid is targeted for the cases with Reynolds number below and including 6 million (low R_{mac}), while the second hybrid grid for the 60 and 120 million cases (high R_{mac}). The third grid consists of purely tetrahedral elements in the volume and triangles on the surfaces. This grid is used for the inviscid computations and is generated by starting with the same surface mesh as the high Reynolds number mesh.

30.4.2.1 Low Reynolds Number Cases

The basic meshing strategy for these cases is to generate a suitable grid for the $R_{mac} = 6 \times 10^6$ case, in terms of first prismatic layer cell height, that can be subsequently used also for the lower Reynolds number cases. The surface discretization is given by isotropic triangular elements over the complete wing and sting. The first prismatic cell height needed to achieve y^+ target values around unity is found to be 1×10^{-6} m for the $R_{mac} = 6 \times 10^6$ case. The viscous layer discretization is realized with up to 32 prismatic layers with a total normal distance to the wall of 0.015 m. An optimal resolution of the viscous sublayer is achieved by setting a non-uniform expansion ratio of 1.17 near to the wall increasing up to 1.3 at the edge of the prismatic layers. The tetrahedral volume discretization is chosen coarse enough to yield first acceptable results. Subsequently, solution based refinement is employed for each case to achieve optimal results. For further details on the initial grid, please refer to Crippa and Rizzi [30-4]. The initial surface grid is visible in Figure 30-2.

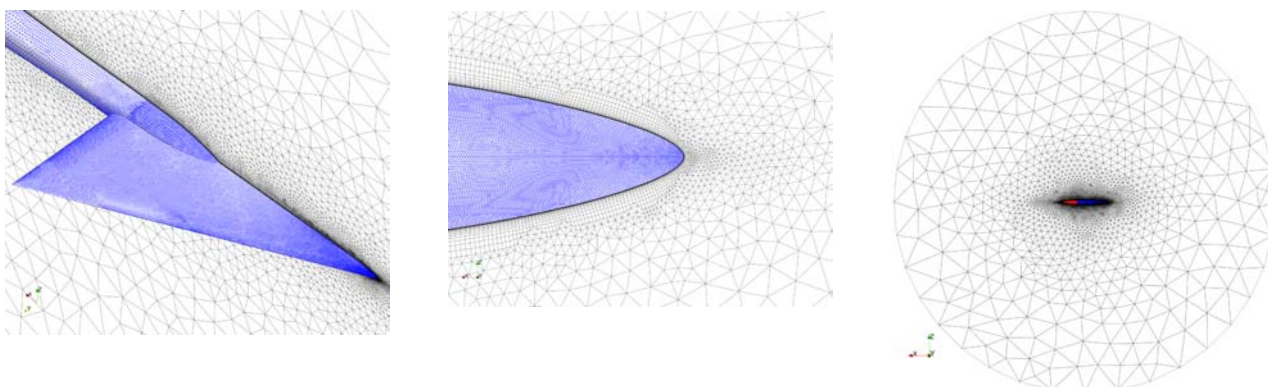

(a) Isometric View **(b) Side View of Apex** **(c) Side View of Symmetry Plane**

Figure 30-2: Initial Blunt Leading Edge Computational Grid for the $R_{mac} = 2 \times 10^6$ and $R_{mac} = 6 \times 10^6$ Cases.

For the solution based mesh refinement at each reference condition, the basic grid is refined using the λ_2 adaptation sensor. The adaptation above the main wing is mainly constrained to the tetrahedral elements by specifying a minimum edge length to be considered for adaptation. An example of the resulting adapted grid is given for the case $\alpha = 13.3°$, $M = 0.4$, $R_{mac} = 3 \times 10^6$. The comparison between the initial surface grid and the adapted grid on the suction side of the wing is shown in Figure 30-3 (a) and Figure 30-3 (b), while the additional tetrahedral cells above the wing are visible in Figure 30-3 (c) and Figure 30-3 (d).

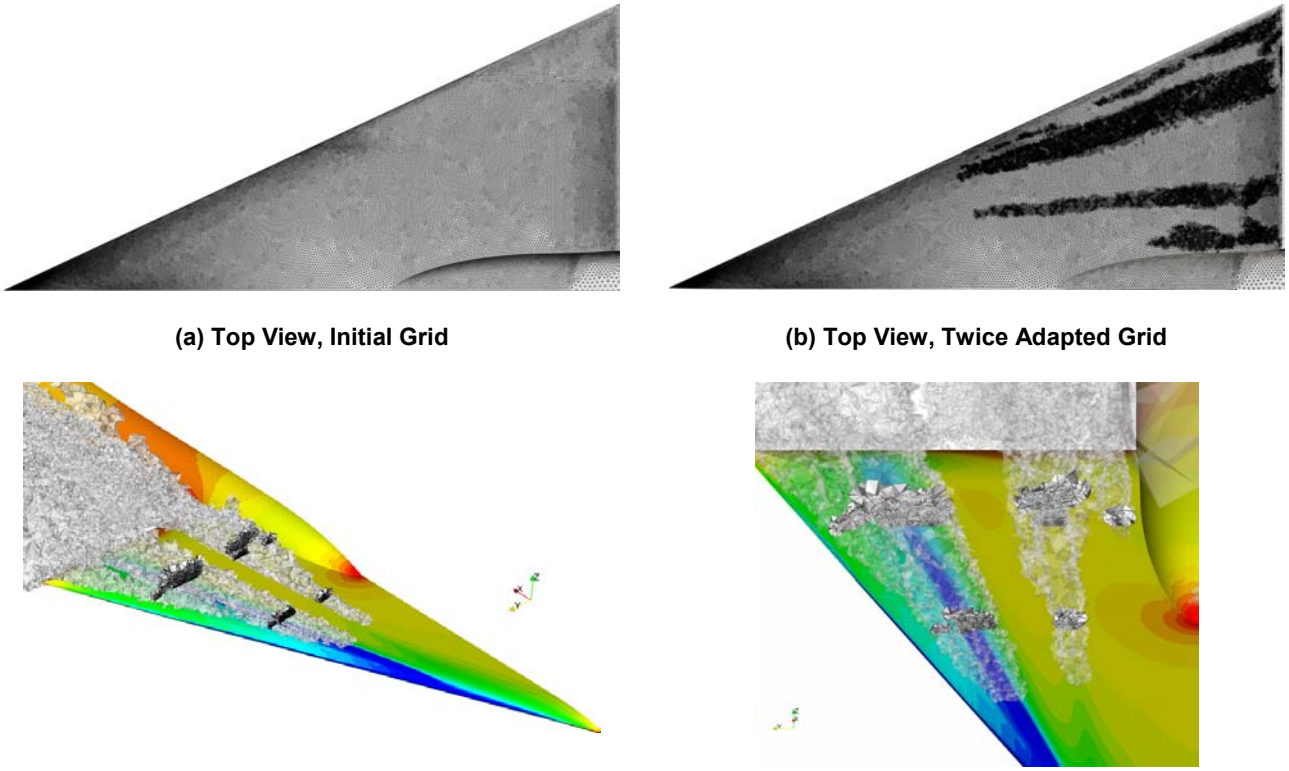

(a) Top View, Initial Grid

(b) Top View, Twice Adapted Grid

(c) Isometric View of C_p on Surface

(d) Front-Upper View of C_p on Surface

Figure 30-3: Comparison of Surface Elements on Suction Side and Additional Tetrahedral Elements after Second Solution-Based Adaptation for Case α = 13.3°, M = 0.4, R_{mac} = 3 x 10^6.

The sensor threshold is set here to the minimum possible value, before several spurious regions are identified within the boundary layer. The additional elements as identified by the λ_2 sensor cluster around four main regions of vortical flow. The largest region of refinement is given by the leading-edge primary vortex. Between the path of the primary vortex and the leading edge it is also possible to discern the adaptation due to the identification of the secondary vortex. Next to the sting it is further possible to see the refinement of the horseshoe-vortex generated by the sting-wing intersection. The fourth identified region is due to an additional inboard vortex, co-rotating with the primary leading-edge vortex, and extensively described by several researchers [30-2],[30-18]. For this study, the correct resolution of this inboard vortex is crucial, but the λ_2 sensor fails here to localize a confined vortical region and thus to refine around the inner vortex upstream of $x/c_r \approx 0.49$. This failure is not due to the specified minimum edge length or the threshold value for the sensor being too high. The vortical motion of the horse-shoe vortex upstream of $x/c_r \approx 0.77$ is also not strong enough to trigger the adaptation sensor. The sizes for the initial grid, as well as the increase in nodes and elements due to the solution based refinement are summarized for each case in Table 30-4. The distribution of refined cells is very similar between the cases. This is mainly due to the relatively high selected sensor threshold value, which resulted in the adaptation algorithm to select and split cell edges beyond the strict region of influence of the main vortical structures. This, coupled to the flow topology for this configuration being similar, resulted in analogue adapted grids for all the different cases.

Table 30-4: Computational Grid Size for the Low R_{mac} Cases – Increase in Comparison to the Initial Grid is Given in Brackets; k = 10^3, M = 10^6 in the Table (Pyramidal elements are included in the total volume nodes counts)

Grid/Case	Total wall surface tri. elements	Prismatic volume cells	Tetrahedral volume cells	Total volume nodes
Initial	172 k	5.25 M	2.36 M	3.09 M
M=0.2, $R_{mac}=2\cdot10^6$	309 k **(80%)**	9.49 M **(80%)**	3.27 M **(39%)**	5.40 M **(75%)**
M=0.4, $R_{mac}=2\cdot10^6$	182 k **(6%)**	5.59 M **(6%)**	2.98 M **(26%)**	3.37 M **(9%)**
M=0.4, $R_{mac}=3\cdot10^6$	278 k **(62%)**	8.65 M **(65%)**	15.71 M **(566%)**	7.07 M **(129%)**
M=0.4, $R_{mac}=6\cdot10^6$	182 k **(6%)**	5.59 M **(6%)**	2.88 M **(22%)**	3.36 M **(9%)**

30.4.2.2 High Reynolds Number Cases

As for the numerical grid of the lower Reynolds number cases, the meshing program TRITET was used also here for producing the volume grid. The surface grid generation was performed again with ANSYS ICEM CFD. This meshing strategy allows for an optimal control of the main delta wing surface resolution. In this case it was modified to better resolve the region of primary separation, expected to shift downstream. This translates into a decrease of triangle density at the apex and an increase at the wing tip. The resolution of the leading edge downstream of $x/c_r = 0.7$ is increased by approx. a factor of three in comparison to the lower Reynolds number grid. The first cell height is 1 x 10^{-7} m, with the total extent of the 36 prismatic layers of 0.003 m, resulting in the non-uniform exponential expansion ratios normal to the wall of 1.21 near the wall and 1.35 at the edge of the prismatic layers.

For the R_{mac} = 60 x 10^6 case, two λ_2 sensor adaptation steps are performed, whereas the first solution-based adaptation for the 120 million R_{mac} case is aimed at achieving a satisfactory y^+ distribution. For this case only one adaptation step was then performed using the λ_2 sensor. See Table 30-5 for the grid size details.

Table 30-5: Computational Grid Size for the High R_{mac} Cases at M = 0.4 – Increase in Comparison to the Initial Grid is Given in Brackets; k = 10^3, M = 10^6 in the Table (Pyramidal elements are included in the total volume nodes counts)

Grid/Case	Total wall surface tri. elements	Prismatic volume cells	Tetrahedral volume cells	Total volume nodes
Initial	199 k	7.17 M	5.50 M	4.57 M
$60\cdot10^6$	289 k **(45%)**	10.38 M **(45%)**	16.61 M **(202%)**	8.08 M **(77%)**
$120\cdot10^6$	579 k **(191%)**	20.84 M **(191%)**	10.29 M **(87%)**	12.33 M **(170%)**

30.4.2.3 Inviscid Case

The same surface mesh as for the high Reynolds number case is used to generate a fully tetrahedral volume grid. The initial mesh is adapted twice using the same λ_2 sensor as for the RANS grids. The sizes of the numerical grids used for the inviscid computations are listed in Table 30-6.

Table 30-6: Computational Grid Size for the Inviscid Case at M = 0.4 – Increase in Comparison to the Initial Grid is Given in Brackets; k = 10^3, M = 10^6 in the Table

Grid	Total wall surface triangular elements	Tetrahedral volume cells	Total volume nodes
Initial	199 k	5.19 M	908 k
Adapted once	358 k (**80%**)	18.51 M (**257%**)	3.19 M (**251%**)
Adapted twice	375 k (**88%**)	23.97 M (**362%**)	4.14 M (**356%**)

30.4.3 Results and Discussion

The maximum and average y^+ values over the delta wing for some relevant cases are presented in Table 30-7.

Table 30-7: Wall-Normal Dimensionless Distance (y^+) on the Delta Wing Surface for the M = 0.4 Cases

R_{mac} [$\cdot 10^6$]	2	3	6	60	120
max y^+	0.44	0.48	0.898	0.648	1.65
mean y^+	0.069	0.096	0.179	0.148	0.41

30.4.3.1 Separation Onset Analysis

Grid size sensitivity is presented here only for case α = 18.5°, M = 0.4, R_{mac} = 6 x 10^6. Furthermore only one set of results is presented in this section from the turbulence model selection runs, relative to the comparison between the CC-EARSM and EARSM models for case α = 18.5°, M = 0.4, R_{mac} = 6 x 10^6.

30.4.3.1.1 18.5° Angle of Attack Cases

The increased prediction accuracy of CC-EARSM over EARSM expected for this type of vortical flows could not be confirmed. Up to x/c_r = 0.4, no difference between the two models could be observed in the pressure coefficient (C_p) plots, but after x/c_r = 0.6 the suction peak associated with the primary vortex is underrepresented by CC-EARSM, see Figure 30-4.

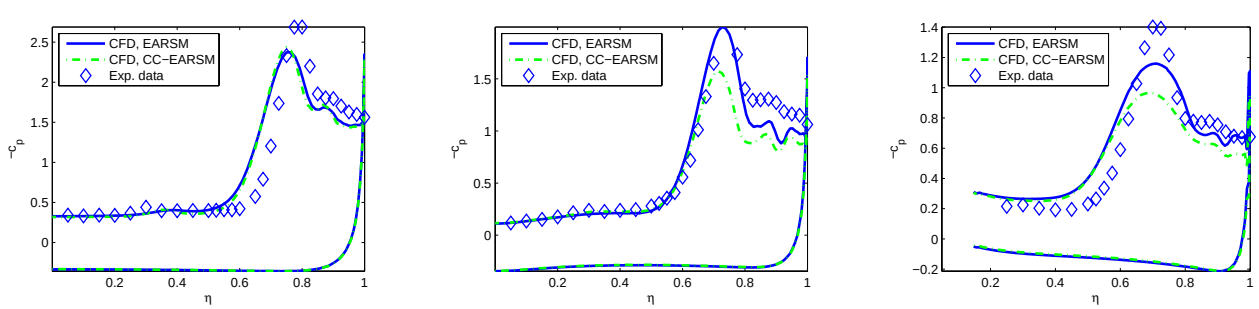

(a) x/c_r = 0.4 **(b) x/c_r = 0.6** **(c) x/c_r = 0.8**

Figure 30-4: C_p Plots for Different x/c_r – Turbulence Model Comparison for Case α = 18.5°, M = 0.4, R_{mac} = 6 x 10^6.

This is disappointing as CC-EARSM should alleviate the need for specific modifications [30-1] to the standard k-ω models, which in the original formulation are known to over-predict the eddy viscosity within vortex cores [30-12]. This led to CC-EARSM not being selected for further computations, but EARSM.

The typical residuals and force coefficients convergence behaviour shown in Figure 30-5 for case $\alpha = 18.5°$, $M = 0.4$, $R_{mac} = 6 \times 10^6$, did not differ substantially from the other cases.

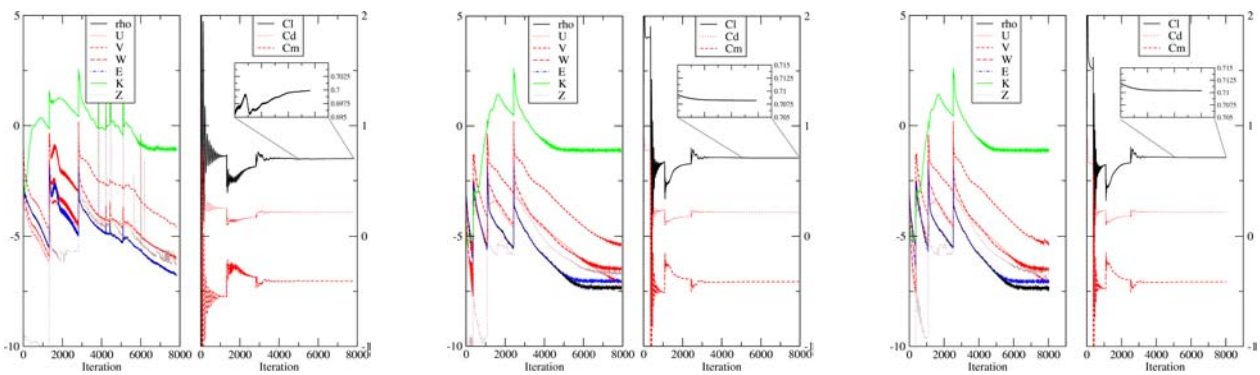

(a) Initial Grid **(b) Once Adapted Grid** **(c) Twice Adapted Grid**

Figure 30-5: Convergence Behaviour for Case $\alpha = 18.5°$, $M = 0.4$, $R_{mac} = 6 \times 10^6$, Scaled Residuals (Logarithmic Scale) and Force Coefficients.

In Figure 30-5 we identify a significantly improved convergence behaviour between the initial and once adapted grid, but no substantial residual convergence gain between the once adapted and twice adapted grid. The increase of lift coefficient (C_L) from 0.7082 for the once adapted grid to 0.7104 for the twice adapted grid is attributed to the stronger primary vortex and thus lower pressure coefficient, see Figure 30-6.

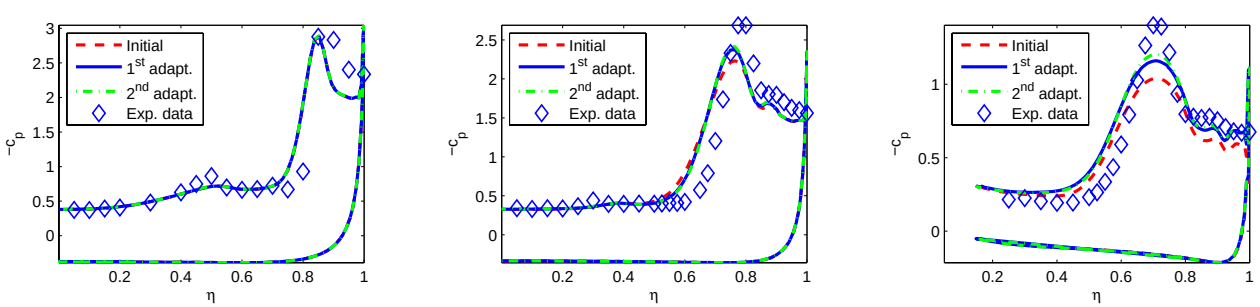

(a) $x/c_r = 0.2$ **(b) $x/c_r = 0.4$** **(c) $x/c_r = 0.8$**

Figure 30-6: C_p Plots for Different x/c_r – Comparison of the Solution on the Initial Grid to Two Further Levels of Refinement and Experimental Data.

Since the main area of interest for this study is in the region of separation onset, the better resolution of the aft section given by the twice adapted grid does not justify the increased computational costs. Thus for the majority of the presented cases, only one adaptation step per case is applied to the initial mesh. If the presented results are achieved on a twice adapted mesh, then it is noted in the relative section. To better interpret the flow structures,

a detailed view of the apex region between approx. $x/c_r = 0.05$ and 0.5 for case $\alpha = 18.5°$, $M = 0.4$, $R_{mac} = 6 \times 10^6$ is shown in Figure 30-7.

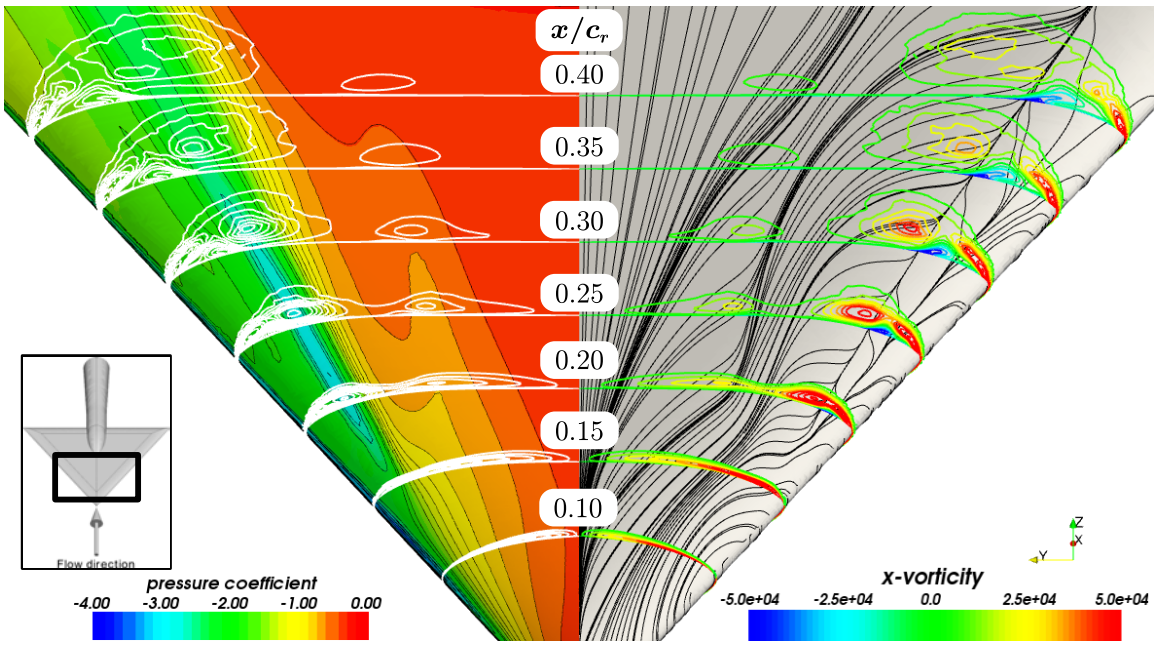

Figure 30-7: Surface Pressure Coefficient, x-Vorticity Iso-Contours and Skin Friction Lines for Case $\alpha = 18.5°$, $M = 0.4$, $R_{mac} = 6 \times 10^6$.

In this figure the surface pressure coefficient is visualized on the left hand side and the skin friction lines on the right hand side. Furthermore, cuts through the flowfield, at constant x/c_r sections, show iso-contours of constant x-component of the vorticity vector. On the right hand side, the same contour curves are colored by the x-vorticity, where positive values indicate a left-handed rotation and negative values a right-handed rotation (in the depicted view). This enables to identify the primary vortex, which is formed at $x/c_r = 0.11$ and a co-rotating vortical structure located further inboard. This structure is dissipated quickly and according to the C_p footprint and the vorticity cuts, it is nearly vanished at $x/c_r = 0.4$.

For case $\alpha = 18.5°$, $M = 0.4$, $R_{mac} = 60 \times 10^6$ a similar phenomenon appears. For this case, the separation onset for both the outer primary vortex, as well as the inner primary vortex is shifted by $x/c_r \approx 5\%$ further downstream. Figure 30-8 depicts the same portion of the delta wing and is structured congruently to Figure 30-7. From this figure it is possible to further identify, based on the skin friction lines, the presence of an inner secondary vortex, developing at approx. $x/c_r = 0.32$.

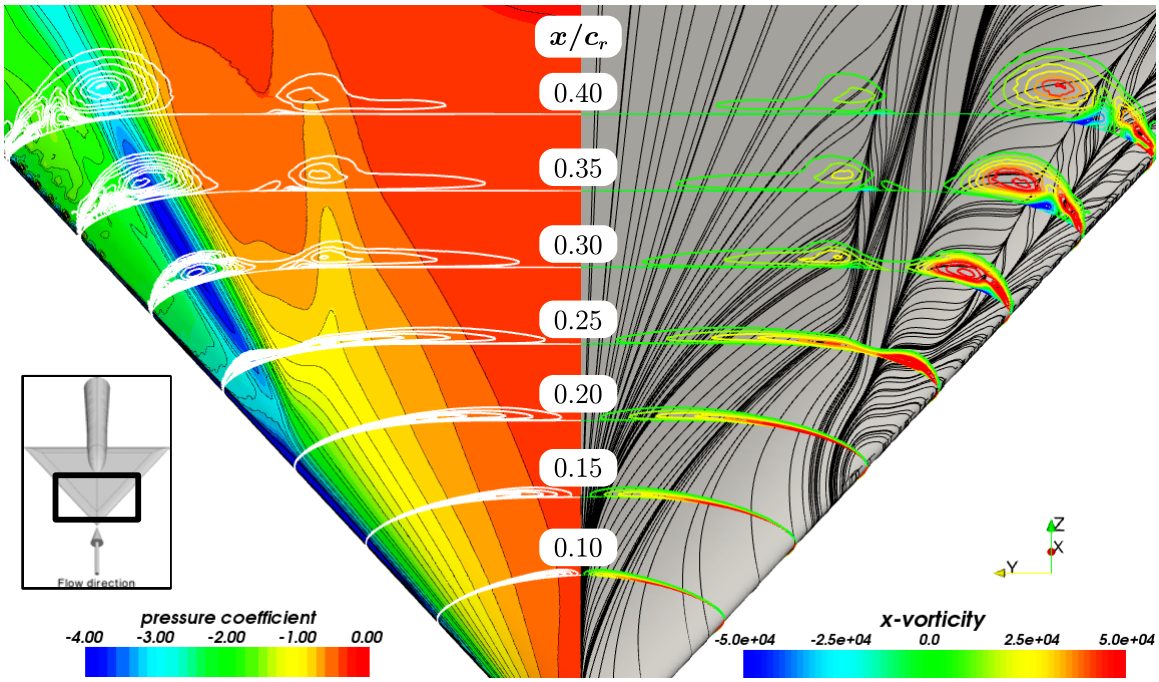

Figure 30-8: Surface Pressure Coefficient, x-Vorticity Iso-Contours and Skin Friction Lines for Case α = 18.5°, M = 0.4, R_{mac} = 60 x 10^6.

The flow topology can be further characterized by identifying separation and attachment lines (SL, AL) of the primary and secondary vortices (PV, SV). The division into inner and outer vortical system (I, O) is added to the description nomenclature of Figure 30-9, e.g., OPVSL corresponds to the outer primary vortex separation line.

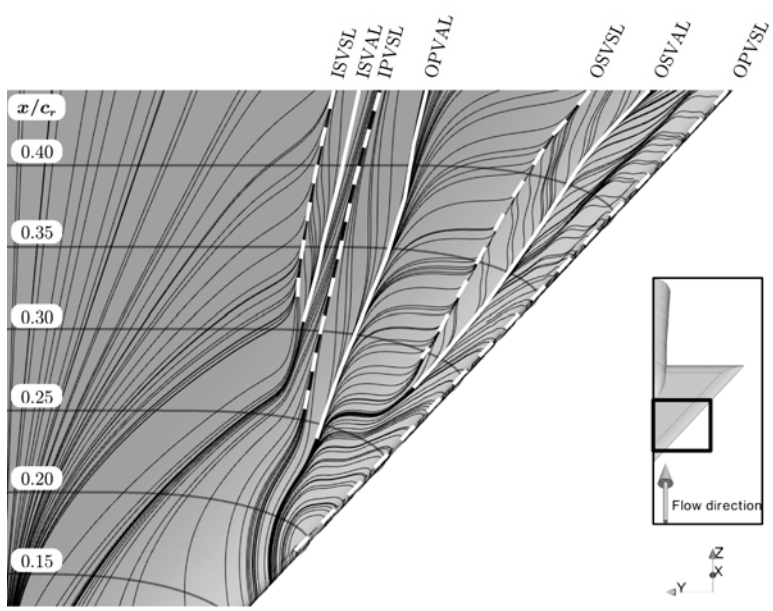

Figure 30-9: Skin Friction Lines and Topological Interpretation – Case α = 18.5°, M = 0.4, R_{mac} = 60 x 10^6.

Note that the inner primary vortex attachment line (IPVAL) is not visible in Figure 30-9, but with the help of spanwise velocity vector cuts (data not shown), it is possible to locate the IPVAL on the symmetry plane.

The pressure coefficient comparison between the computed case at R_{mac} = 60 x 10^6 and experimental data shows good agreement, see Figure 30-10. This is mainly due to the small discrepancy between computed and experimental separation onset of the primary and inner vortices. The computations seem to over-predict the vortex strength, as visible on the C_p plot for x/c_r = 0.95, see Figure 30-10 (d).

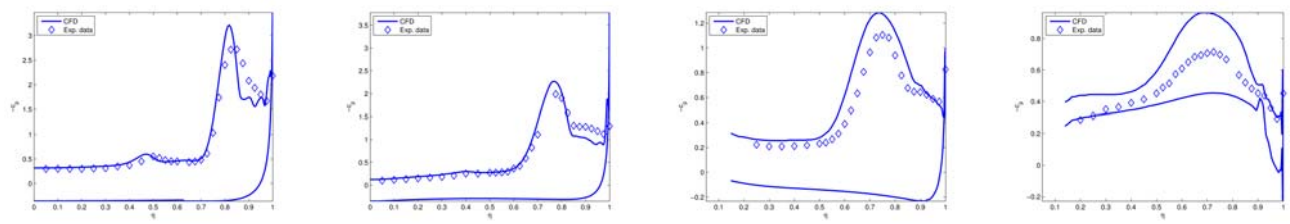

(a) x/c_r = 0.4 **(b) x/c_r = 0.6** **(c) x/c_r = 0.8** **(d) x/c_r = 0.95**

Figure 30-10: C_p Plots for Different x/c_r – Case α = 18.5°, M = 0.4, R_{mac} = 60 x 10^6.

30.4.3.1.2 23.0° Angle of Attack Cases

The sensitivity of the flowfield to the primary vortex separation location as shown for the α = 18.5° cases is expected to decrease when increasing the angle of attack. This is here the case, as visible in Figure 30-11, where for the α = 23.0° cases the outer primary vortex develops within a short distance from the apex, at about x/c_r = 0.1.

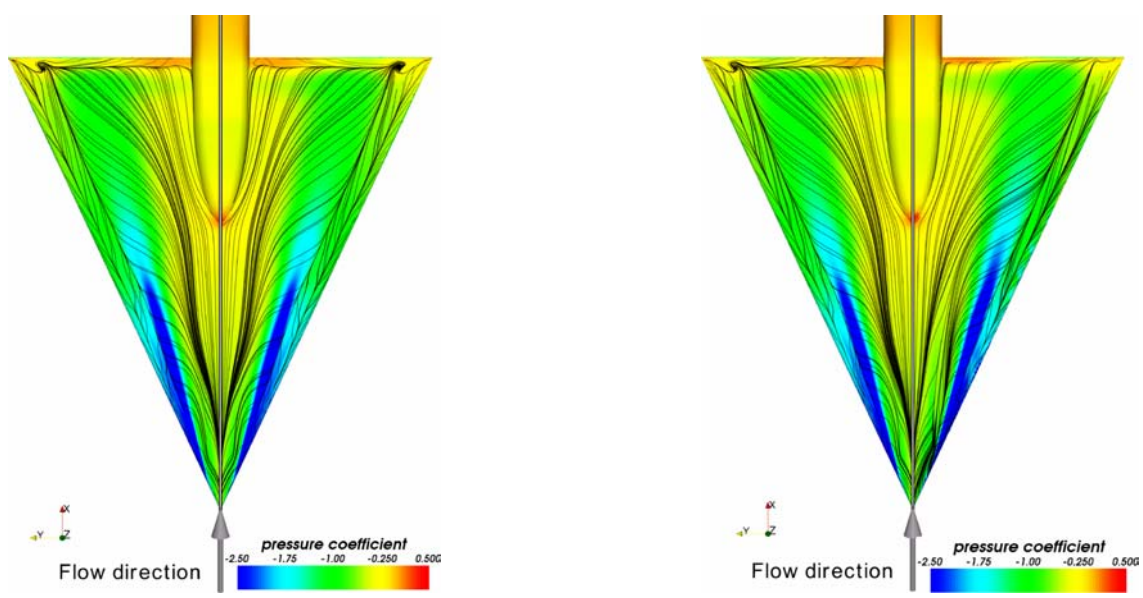

(a) Left Frame: R_{mac} = 6 x 10^6; Right Frame: R_{mac} = 2 x 10^6 **(b) Left Frame: R_{mac} = 6 x 10^6; Right Frame: R_{mac} = 60 x 10^6**

Figure 30-11: Surface Pressure Coefficient – View on the Suction Side, Perpendicular above the Flat Delta Wing Central Part; α = 23.3°, M = 0.4.

The same viewpoint and visualization technique as for case α = 18.5°, M = 0.4, R_{mac} = 60 x 10^6 (Figure 30-8) can be used to identify a similar flow topology for case α = 23.0°, M = 0.4, R_{mac} = 60 x 10^6.

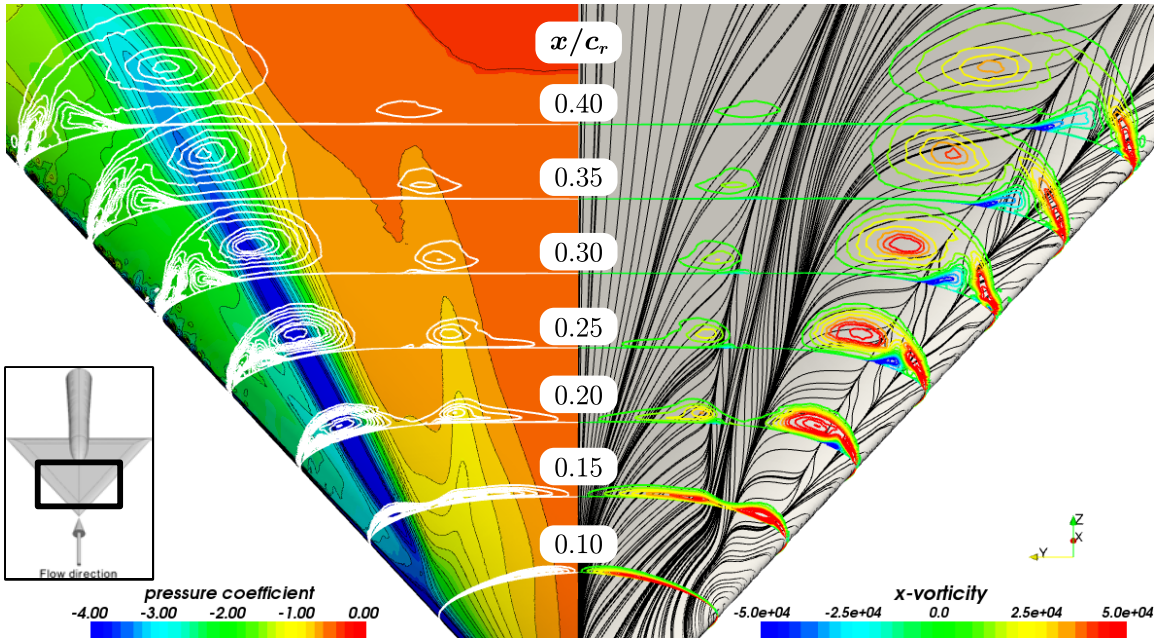

Figure 30-12: Surface Pressure Coefficient, x-Vorticity Iso-Contours and Skin Friction Lines for Case α = 23.3°, M = 0.4, R_{mac} = 60 x 10^6.

Again, the skin friction pattern, combined with the iso-contours of x-vorticity at specific cuts reveals the presence of an inner primary and secondary vortex system. In contrast to case α = 18.5°, M = 0.4, R_{mac} = 60 x 10^6, here this system is dissipated relatively quickly and as soon as x/c_r = 0.3 the inner secondary attachment line detaches from the surface. This happens also for the inner secondary vortex separation line at x/c_r = 0.34. These observations are summarized in Figure 30-13 (a), where separation and attachment lines for both inner and outer vortical system are sketched.

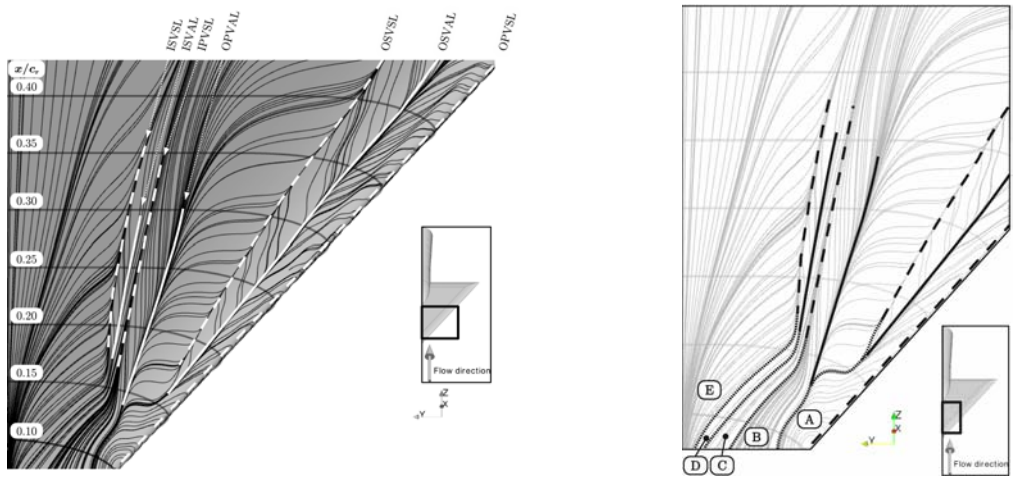

(a) Skin Friction Lines and Topological Interpretation **(b) Zonal Subdivision**

Figure 30-13: Skin Friction Lines and Topological Interpretation – α = 23.3°, M = 0.4, R_{mac} = 60 x 10^6.

For this AOA the CFD data is found to match best the experimental data, as can be seen in the C_p plots presented in Figure 30-14 for case α = 23.0°, M = 0.4, R_{mac} = 2 x 10^6, in Figure 30-15 for case α = 23.0°, M = 0.4, R_{mac} = 6 x 10^6 and in Figure 30-16 for case α = 23.0°, M = 0.4, R_{mac} = 60 x 10^6. At this incidence, as for the α = 18.5° case, the R_{mac} = 60 x 10^6 case matches best the experimental data.

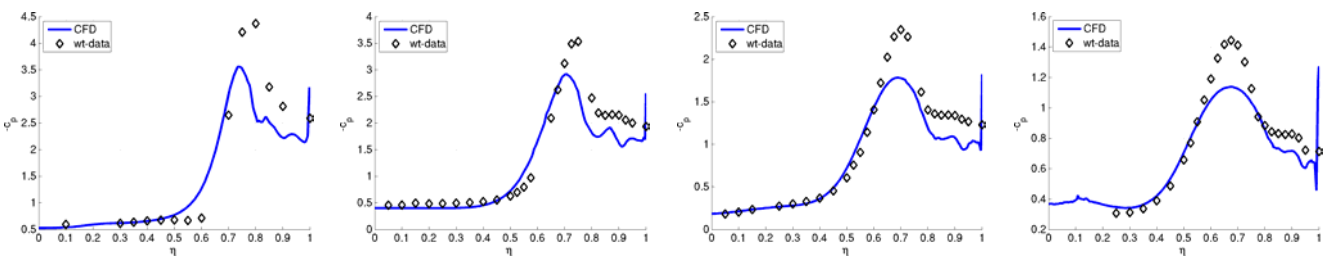

(a) x/c_r = 0.2 **(b) x/c_r = 0.4** **(c) x/c_r = 0.6** **(d) x/c_r = 0.8**

Figure 30-14: C_p Plots for Different x/c_r – Case α = 23.3°, M = 0.4, R_{mac} = 2 x 10^6.

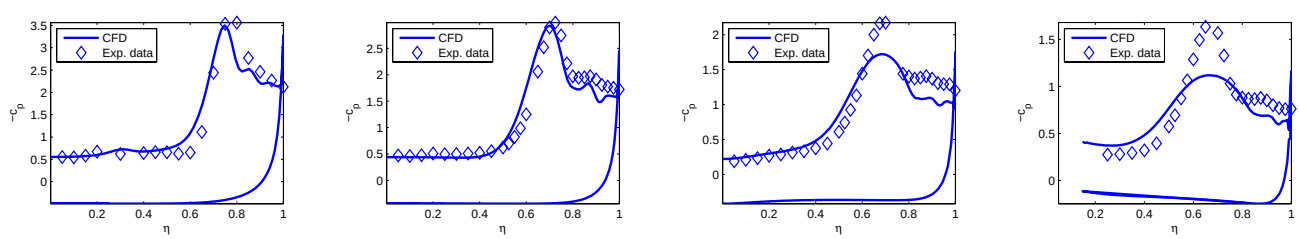

(a) x/c_r = 0.2 **(b) x/c_r = 0.4** **(c) x/c_r = 0.6** **(d) x/c_r = 0.8**

Figure 30-15: C_p Plots for Different x/c_r – Case α = 23.3°, M = 0.4, R_{mac} = 6 x 10^6.

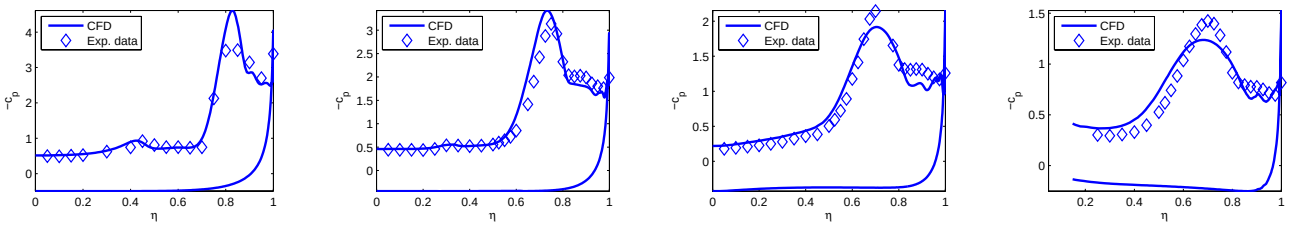

(a) $x/c_r = 0.2$ (b) $x/c_r = 0.4$ (c) $x/c_r = 0.6$ (d) $x/c_r = 0.8$

Figure 30-16: C_p Plots for Different x/c_r – Case α = 23.3°, M = 0.4, R_{mac} = 60 x 10^6.

30.4.3.1.3 Conclusions

The location of primary vortex separation onset can be determined in two ways. A simple, graphical method, when fine-grained leading edge pressure measurements are not available, is to geometrically extend the location of the primary vortex core path upstream, to intersect the leading edge and mark this intersection as the separation onset. Another, more accurate, possibility is to evaluate the skin friction lines in the vicinity of the leading edge to identify the position, where convergence of two skin friction lines occurs first. This position determines the so-called squeeze-off separation onset location. For comparison, both methods are used here to determine the separation onset. The error of the vortex core prolongation method is minimal. For all cases, both methods give similar results. These are compared with experimental data and summarized in Figure 30-17. At the lowest Reynolds number and lowest incidence the agreement is worst. Going from the R_{mac} = 6 x 10^6 to the R_{mac} = 60 x 10^6 cases, the agreement increases. With the R_{mac} = 60 x 10^6 cases fitting best by considering the percental difference between CFD and experimental data.

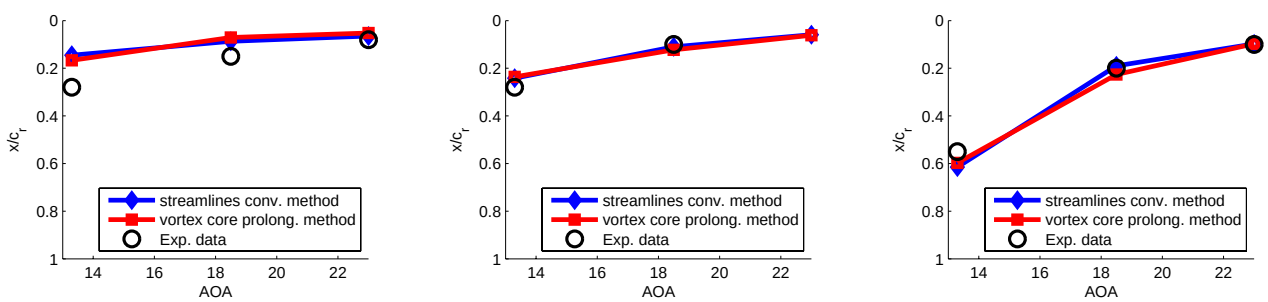

(a) R_{mac} = 2 x 10^6 (b) R_{mac} = 6 x 10^6 (c) R_{mac} = 60 x 10^6

Figure 30-17: Outer Primary Vortex Separation Onset.

Since the separation onset of the inner primary vortex is not as clear for the α = 13.3° and all R_{mac} = 2 million cases, only the results for R_{mac} = 60 million and for the cases at higher AOA at R_{mac} = 6 million are presented in Figure 30-18. Comparison between computed and measured results is not possible here, due to unavailability of experimental data. The relatively constant distance between outer and inner primary vortex separation onset is an indication that these vortical systems are closely coupled.

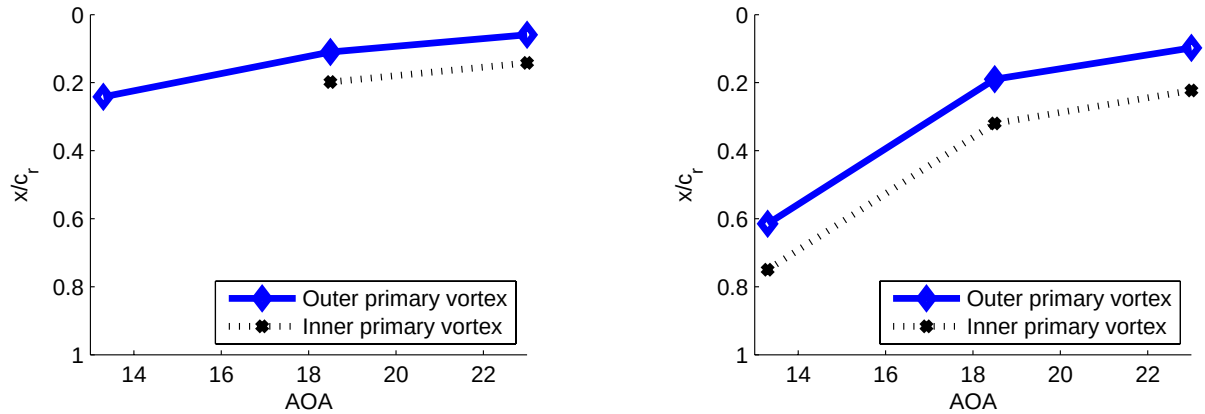

(a) R_{mac} = 6 x 10^6 **(b) R_{mac} = 60 x 10^6**

Figure 30-18: Inner and Outer Primary Vortex Separation Onset.

The predicted outer primary separation onset location is shown to match well the data from experimental investigations at high Reynolds numbers. This enables to gain certainty in the determination of the inner primary vortex separation, which is shown to correlate with the outer primary vortex separation and attachment. This is especially true for the high AOA, high R_{mac} case (case α = 23.0°, M = 0.4, R_{mac} = 60 x 10^6), where the coupling between outer primary vortex attachment line (onset and length) with the inner primary vortex separation line (onset and length) is clearly recognizable. The primary vortex attachment line (OPVAL in Figure 30-12) separates the diverging streamlines passing under the outer primary vortex on one side (pointing outboard, region "A" in Figure 30-13 (b)) and the streamlines being diverted towards the centreline on the other side (region "B" in Figure 30-13 (b)). The onset of the inner primary vortex (IPVSL in Figure 30-13 (a)) coincides where the streamlines diverted towards the centreline by the outer primary vortex hit for the first time the further upstream, inboard streamlines from the delta wing apex region ("C" in Figure 30-13 (b)). If the inner primary vortex strength is predicted well, the attached flow passing under the inner primary vortex core (coming from regions "D" and "E" in Figure 30-13 (b)) is accelerated sufficiently to trigger (inner) secondary separation. Where the outer primary vortex attachment on the surface is not present anymore (for case α = 23.0°, M = 0.4, R_{mac} = 60 x 10^6 at x/c_r = 0.30), the inner vortex starts to decrease in strength and shortly after (for case α = 23.0°, M = 0.4, R_{mac} = 60 x 10^6 at x/c_r = 0.34) the inner primary vortex separation stops.

Although the numerical results for the R_{mac} = 6 x 10^6 cases do not match well the experimental data, the inner primary vortex separation mechanism described above can be recognized also here (e.g., case α = 18.5°, M = 0.4, R_{mac} = 6 x 10^6). Both the outer primary vortex strength and the outer primary vortex attachment line extent are under-predicted. In this case the diversion of the streamlines from the outer primary vortex attachment line towards the centreline is not as strong as it is in reality. Thus the coincidence between these streamlines and the further inboard streamlines (for case α = 18.5°, M = 0.4, R_{mac} = 6 x 10^6 at x/c_r = 0.22) induces only a weak inner primary vortex, which does not trigger secondary separation. From the above discussion, it is clear that the numerical method used for this study is shown to perform best at the higher AOA of 23.0° and R_{mac} of 60 million for resolving the double vortex system.

30.4.3.2 Flow Topological Analysis

This section contributes to the common effort to describe the flow phenomena for the co-rotating double-vortex system. This is done by highlighting the strengths and deficiencies encountered by steady CFD computations at low Reynolds numbers around the nominal angle of attack of 13.3°, and subsonic Mach number, M = 0.4.

For these free-stream conditions, the leading-edge normal AOA and Mach number are α_N = 29.22° and M_N = 0.19. Even though the classification by Eberle et al. [30-6] does not account for the effects of Reynolds number, it differentiates between sharp and blunt leading-edged, slender delta wings. The flow pattern to be expected for the considered case can be extracted from the α_N-M_N classification [30-6]. For the conditions as given above, the data point lies in the middle of the region denominated "development of vortex system". In this condition, a higher Reynolds number would shift the data point towards the fully attached flow region by delaying the separation onset; whereas a lower Reynolds number would eventually result in the appearance of fully developed vortices. The sensitivity of this case to small variations of Reynolds number, AOA and free-stream Mach number makes it a challenging case for computational methods. Thus the numerical exploration of a wide range of Reynolds numbers and a topological flow analysis are the main topics of this study.

30.4.3.2.1 Surface Pressure Coefficient

A comparison of computed surface pressure data to experimental pressure sensitive paint (PSP) data from Konrath et al. [30-17] is here only possible for the $R_{mac} = 3 \times 10^6$ case. This is presented in Figure 30-19 (to be compared against Figure 30-21(c)). The surface pressure coefficient plots of the delta wing suction side are presented in Figure 30-20 for the inviscid computation and in Figure 30-21 for the viscous computations.

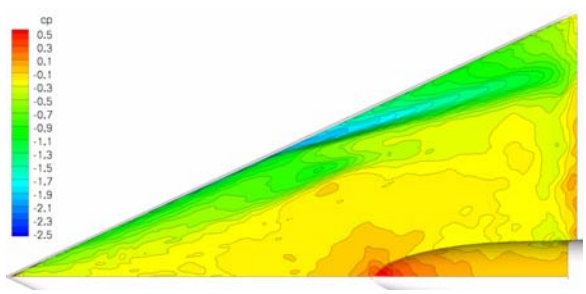

Figure 30-19: Experimental Pressure Coefficient Surface Plot for α = 13.3°, M = 0.4, $R_{mac} = 3 \times 10^6$ Data Provided by DLR [30-17].

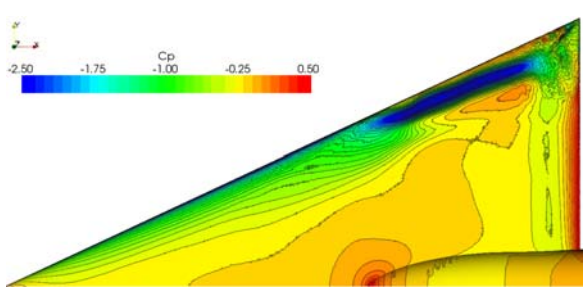

Figure 30-20: Surface Pressure Coefficient on Half-Span Suction Side – CFD Result for the Inviscid Case.

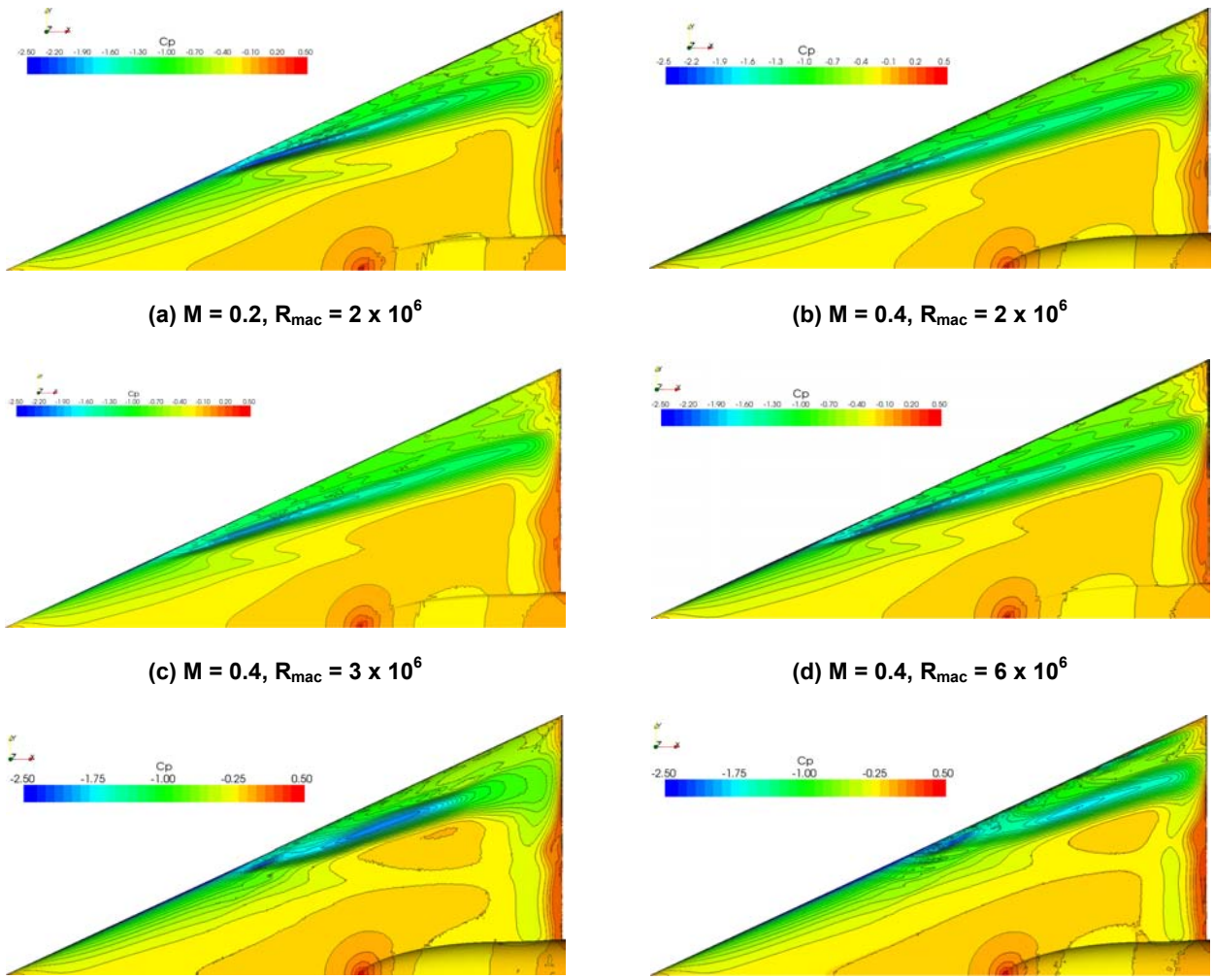

(a) M = 0.2, R_{mac} = 2 x 10^6

(b) M = 0.4, R_{mac} = 2 x 10^6

(c) M = 0.4, R_{mac} = 3 x 10^6

(d) M = 0.4, R_{mac} = 6 x 10^6

(e) M = 0.4, R_{mac} = 60 x 10^6

(f) M = 0.4, R_{mac} = 120 x 10^6

Figure 30-21: Surface Pressure Coefficient on Half-Span Suction Side – CFD Results for the Viscous Cases.

The trends as described by Luckring [30-23] in respect to Reynolds number and compressibility dependence are also found when examining the computational results. The effect of an increase of Mach number on the upstream movement of primary separation onset is shown here from M = 0.2 to M = 0.4 (Figure 30-21(a) to Figure 30-21(b)). The opposite effect for an increase of Reynolds number, i.e. delay of primary separation onset, is clear when comparing Figure 30-21(b) to Figure 30-21(f).

The inviscid case features a substantially stronger primary vortex than the highest Reynolds number case. From analysis of the surface pressure data it forms at $x/c_r \approx 0.6$ and is located too far outboard. But the overall picture is as expected from an inviscid computation.

30.4.3.2.2 Span-Wise Pressure Coefficient

The half-span surface pressure coefficient graphs are presented here only for the cases with available experimental data and are normalized by the local semi-span to give the local non-dimensional semi-span (η). For all cases considered in this study, at $x/c_r = 0.2$ the computations agree with the experimental data in predicting fully attached flow. Thus the foremost available location from the experimental datasets ($x/c_r = 0.2$) is not presented hereafter.

The viscous computations are presented in Figure 30-22 to Figure 30-25, while the inviscid case is only compared to other viscous cases in Figure 30-26 and Figure 30-27.

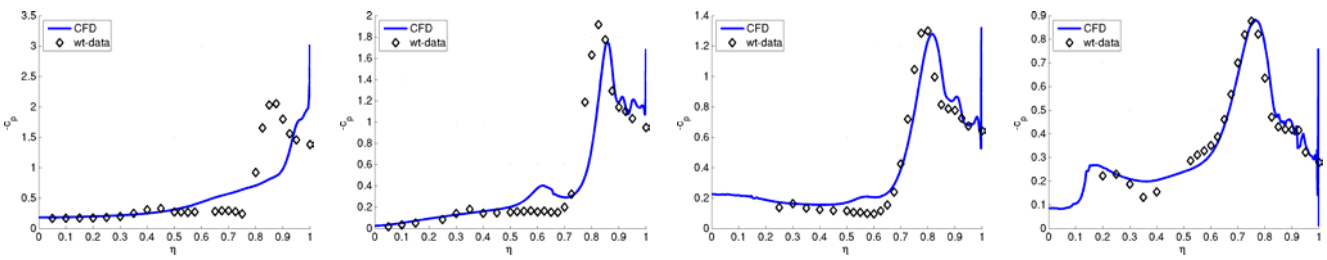

(a) $x/c_r = 0.4$ **(b) $x/c_r = 0.6$** **(c) $x/c_r = 0.8$** **(d) $x/c_r = 0.95$**

Figure 30-22: C_p Plots for Different x/c_r – Case α = 13°, M = 0.2, $R_{mac} = 2 \times 10^6$ – Comparison between CFD Results and Experimental Data [30-17].

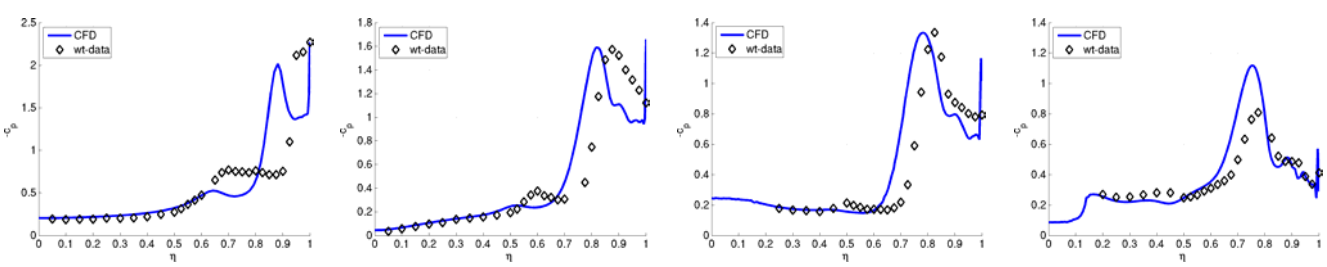

(a) $x/c_r = 0.4$ **(b) $x/c_r = 0.6$** **(c) $x/c_r = 0.8$** **(d) $x/c_r = 0.95$**

Figure 30-23: C_p Plots for Different x/c_r – Case α = 13.3°, M = 0.4, $R_{mac} = 6 \times 10^6$ – Comparison between CFD Results and Experimental Data [30-3].

30.4.3.2.3 Effect of Turbulence Modelling

The only results presented in this section for the turbulence model comparison are between the CC-EARSM and EARSM models for the case α = 13.3°, M = 0.4, $R_{mac} = 3 \times 10^6$, as the observed behaviour is similar for the other cases. Other examined turbulence models affected the location of primary vortex separation onset; in some cases positively as for the one-equation Spalart-Allmaras model and in other cases negatively as for the standard Wilcox k-ω model. None of the evaluated models correctly resolves the initial formation of the inner vortex. A motivation for the assessment of curvature corrected models is that a better resolution of the inner vortex was hoped for. Up to $x/c_r = 0.2$, no difference between the two models can be observed in the pressure coefficient (C_p) plots, but right after the formation of the primary vortex the main suction peak is

stronger, as expected from CC-EARSM, see Figure 30-24 (a) and Figure 30-24 (b). At $x/c_r = 0.8$ CC-EARSM shows a weaker primary suction peak and at $x/c_r = 0.95$ no major difference between the two models is seen in regards to primary suction peak. Although CC-EARSM initially performs as expected in regards to primary vortex strength, the inner vortex is under-predicted over the complete path. The difference to EARSM is only minor, but visible in Figure 30-24 (a), where at $\eta \approx 0.6$, it is possible to recognize the weaker inner vortex suction peak for the CC-EARSM case.

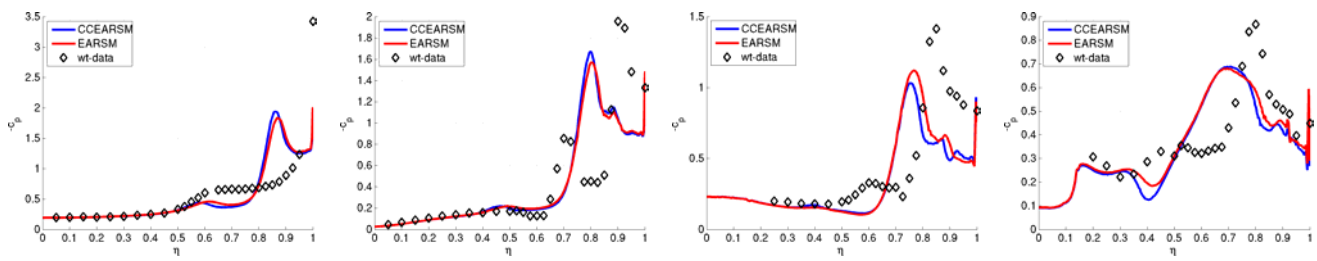

(a) $x/c_r = 0.4$ **(b) $x/c_r = 0.6$** **(c) $x/c_r = 0.8$** **(d) $x/c_r = 0.95$**

Figure 30-24: C_p Plots for Different x/c_r – Case $\alpha = 13.3°$, $M = 0.4$, $R_{mac} = 3 \times 10^6$ – Comparison between CFD Results and Experimental Data [30-3].

30.4.3.2.4 Effect of Mesh Refinement

The effect of solution-based mesh refinement on the solution accuracy is presented here only exemplary for the case $R_{mac} = 60 \times 10^6$. As displayed in Figure 30-25, a substantial improvement is found through the first adaptation step. A second adaptation does not result in an equally pronounced improvement over the majority of the wing. Only at $x/c_r = 0.95$ a difference is visible between the second and first adaptation step. This behaviour is found in all other evaluated cases, where a single adaptation step is sufficient.

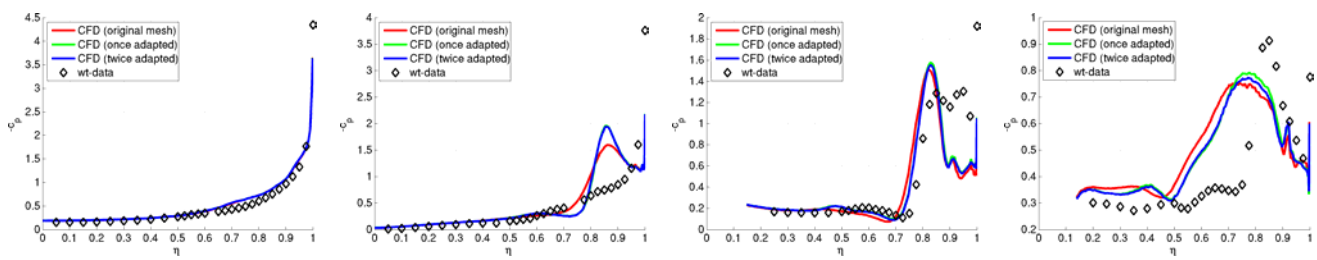

(a) $x/c_r = 0.4$ **(b) $x/c_r = 0.6$** **(c) $x/c_r = 0.8$** **(d) $x/c_r = 0.95$**

Figure 30-25: C_p Plots for Different x/c_r – Case $\alpha = 13.3°$, $M = 0.4$, $R_{mac} = 60 \times 10^6$ – Comparison between CFD Results and Experimental Data [30-17].

From the analysis of the available comparisons, it is obvious that the CFD computations consistently disagree with the experimental datasets in terms of separation onset of the primary leading-edge vortex. In all evaluated cases the separation onset of the primary vortex is predicted too far upstream, resulting in an inboard shift of the primary vortex suction peak in all sections downstream of separation onset. The typical over-prediction of secondary separation strength is also observed.

The inner vortical system is captured in all cases, but the location and strength are predicted wrongly. For the $\alpha = 13.3°$, $M = 0.4$, $R_{mac} = 2 \times 10^6$ case, the strength of the inner vortex is over-predicted in comparison to the experimental data (Figure 30-22). However, Figure 30-23 (a) to Figure 30-23 (c) and Figure 30-24 (a) to Figure 30-24 (c) present evidence of an under-prediction of inner vortex strength for the low Reynolds number, M = 0.4 cases. A feature that is missed consistently in all computational results is the span-wise extent of a low-pressure region just upstream of the primary leading-edge vortex separation onset, which extends from $\eta \approx 0.65$ to $\eta \approx 0.85$ (Figure 30-23 (a) and Figure 30-24 (a)). This difference is also discernible when comparing the experimental PSP data from Konrath et al. [30-17] in Figure 30-19 to the corresponding computed case in Figure 30-21 (c). None of the computed cases feature such an extended C_p plateau prior to leading-edge separation onset as experienced in the experimental campaigns.

The delaying effect of Reynolds number on the primary vortex separation onset is appreciated in Figure 30-26. A coupling between the primary vortex separation onset and the growth of inner vortex strength, as described by Crippa and Rizzi [30-4] and presented in previous sections, is observed in Figure 30-27. It is also possible to discern the presence of a weak suction peak in Figure 30-27 (d) at $\eta \approx 0.55$ for the inviscid case.

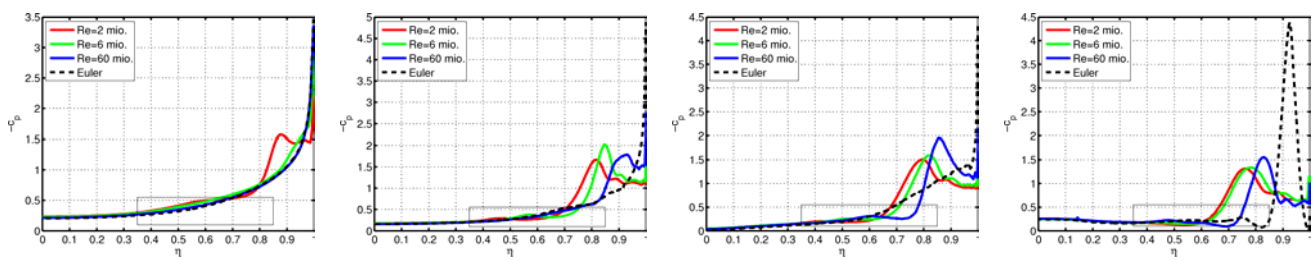

(a) $x/c_r = 0.3$ **(b) $x/c_r = 0.5$** **(c) $x/c_r = 0.6$** **(d) $x/c_r = 0.8$**

Figure 30-26: C_p Plots for Different x/c_r – Case $\alpha = 13.3°$, M = 0.4 – Comparison of CFD Results for Different Reynolds Numbers and Inviscid Computation.

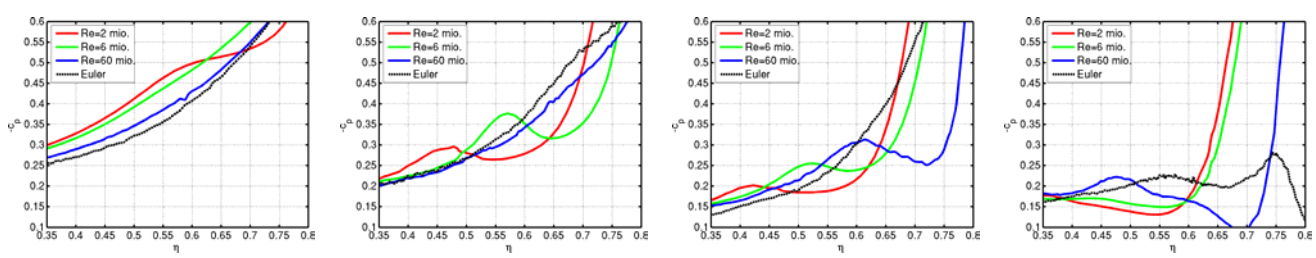

(a) $x/c_r = 0.3$ **(b) $x/c_r = 0.5$** **(c) $x/c_r = 0.6$** **(d) $x/c_r = 0.8$**

Figure 30-27: C_p Plots for Different x/c_r – Case $\alpha = 13.3°$, M = 0.4 – Comparison of CFD Results for Different Reynolds Numbers and Inviscid Computation – Magnification on Inner Vortical Region.

30.4.3.2.5 Flow Topology

Despite the differences between the computational and the experimental results, the off-body vortical structures are analyzed to understand the formation of the inner vortex as well as its coupling to the primary leading-edge vortex formation. For this purpose the case at $M = 0.2$, $R_{mac} = 2 \times 10^6$ is presented hereafter, since it features the strongest inner vortex.

All the skin friction lines from the symmetry plane to the leading-edge secondary attachment line can be traced upstream to a very confined region at the apex, highlighted in Figure 30-28 (a) and presented Figure 30-28 (b). The attachment on the suction side from the symmetry plane at $x/c_r \approx 0.01$ at the half-saddle point C diverts the streamlines originating from the primary attachment line on the pressure side of the wing, see Figure 30-28 (b), where the centre-most skin friction line (St1) is parallel to the symmetry plane upstream of the attachment half-saddle point C. Downstream of the attachment half-saddle point C, St1 remains parallel to the streamlines emanating from C, see for example St2. This surface topology was found on all cases, whereby the location of C moves towards the apex as the Reynolds number increases.

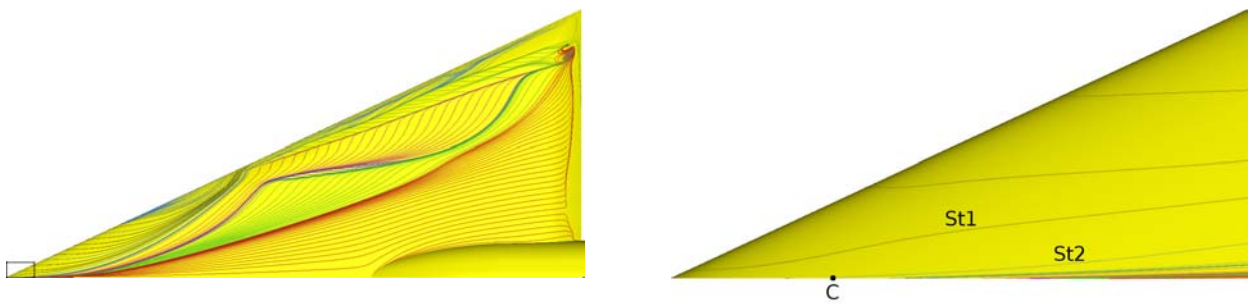

(a) Complete Wing with Magnification Region at Apex

(b) Magnified Region, $x/c_r \approx 0 – 0.01$

Figure 30-28: M = 0.2, $R_{mac} = 2 \times 10^6$ – Color-Coded Skin Friction Lines on Suction Side.

The isometric view presented in Figure 30-29 (a) gives further insight in the off-body flow topology. From the trajectories at $x/c_r = 0.2$ it is possible to discern a weak vortical motion extending from the symmetry plane to $\eta \approx 0.5$ (Figure 30-29 (b)). The attachment line of this vortex is shown on the symmetry plane by the iso-line of zero wall-normal velocity. This vortical structure extends for this case from $x/c_r \approx 0.1$ to $x/c_r \approx 0.85$, where it merges with the primary leading-edge vortex. For this case, the onset of squeeze-off separation that leads to the formation of the leading-edge primary vortex happens at $x/c_r \approx 0.215$. This is downstream of the formation of the vortical structure near the centreline, the formation of which coincides with the foremost position of the iso-line of zero wall-normal velocity.

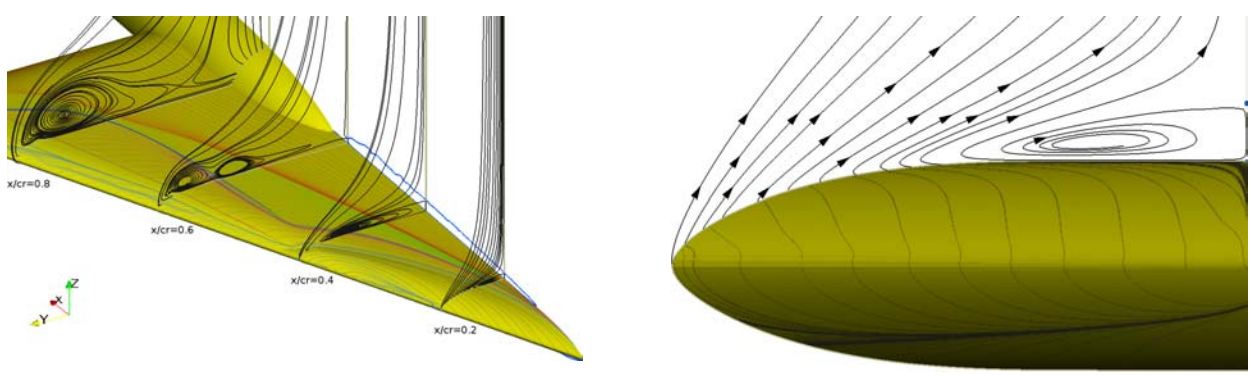

(a) Isometric View – Inner Vortex Attachment Line is Shown on the Symmetry Plane

(b) Frontal View of Trajectories Projected on Plane $x/c_r = 0.2$ and Surface Streamlines

Figure 30-29: M = 0.2, $R_{mac} = 2 \times 10^6$ – Skin Friction Lines and Field Lines of Force Projected on x/c_r Planes.

The presence of a thin vortical structure upstream of primary leading-edge separation onset is documented experimentally by Konrath et al. [30-18]. The PIV data for case $\alpha = 13.3°$, $M = 0.4$, $R_{mac} = 3 \times 10^6$ at $x/c_r = 0.35$ is presented in Figure 30-30 (a) next to the computed case at the same conditions Figure 30-30 (b). Compared to the experimental data, the computations show a wider and flatter vortex. The span-wise extent of the computed vortex is approx. 75% of the local semi-span. A direct comparison to the experimental data is in this respect not possible since the PIV field does not reach the symmetry plane, but the vortex core location is visible. In the computations it is too far inboard by as much as 12% of the semi-span. However, the total surface-integrated vorticity is comparable between the computations and experiments. The observed discrepancy in location and extent of the apex vortex is believed to be the reason for the absence in the computations of the low-pressure plateau as presented in Section 30.4.3.2.2. A thicker, further outboard concentrated vortex could explain this C_p plateau.

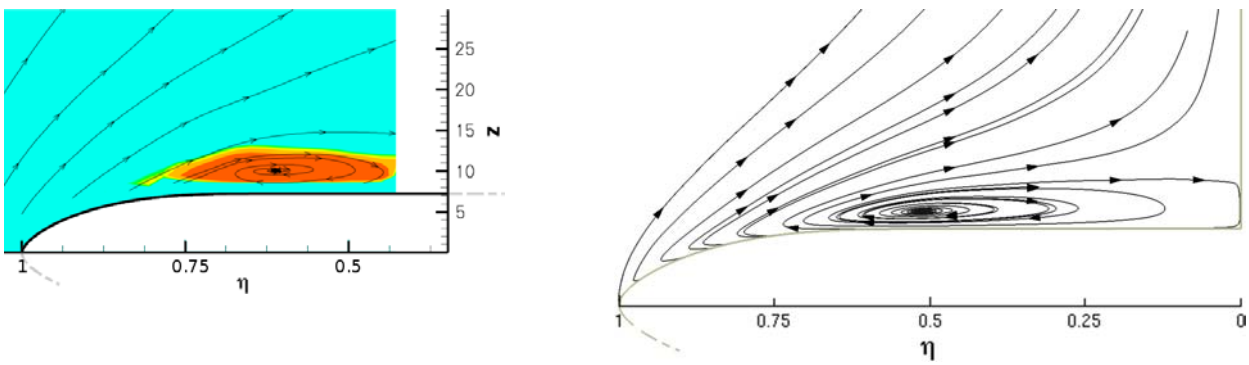

(a) Experimental Time-Averaged Vorticity Magnitude and Field Lines of Force – Data Provided by DLR [30-18]

(b) Field Lines of Force for the CFD Results.

Figure 30-30: $\alpha = 13.3°$, $M = 0.4$, $R_{mac} = 3 \times 10^6$ – Cut Plane at $x/c_r = 0.35$.

The skin friction lines on the suction side of the wing presented in Figure 30-28 reveal a distinct separation line inboard of the primary vortex attachment line. This separation line extends from $x/c_r \approx 0.48$ to $x/c_r \approx 0.66$ and is difficult to classify without detailed off-body flow analysis. Through vorticity-colored cut-planes and interactive placement of streamlines, this separation line can be attributed to a secondary vortex. The formation of which is due to the very strong inner vortex. At higher incidences, this feature was already found numerically by Crippa and Rizzi [30-4], while at the lower incidences it is only documented experimentally at similar conditions by Furman and Breitsamter [30-11] (see Figure 30-31).

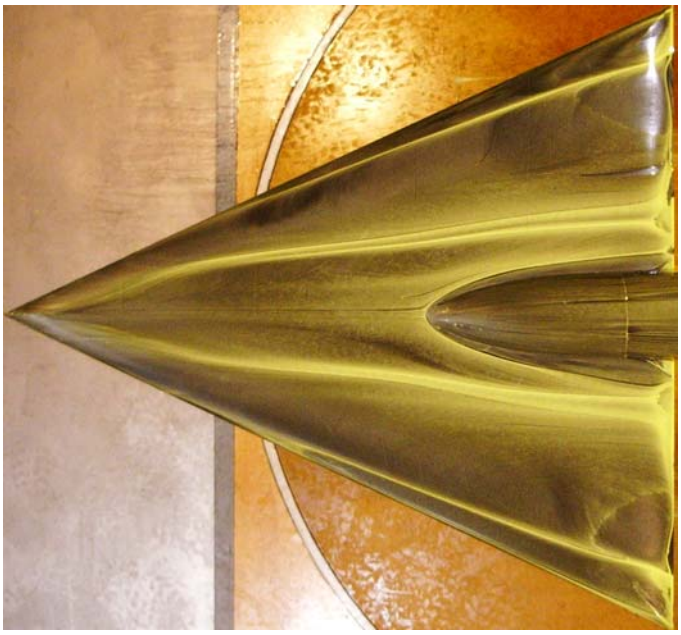

Figure 30-31: Oil-Flow Image of Blunt Leading-Edge Suction Side – $\alpha = 13°$, $M = 0.14$, $R_{mac} = 2 \times 10^6$ (Reproduced with permission [30-11]).

In the experimental campaign, the extension of this inner separation line was coupled to an equally distinct inner attachment line, attributed to the inner vortex, originating in the apex region. The extent of the inner separation and attachment lines was found to span from $x/c_r \approx 0.27$ to the trailing edge and located inboard of $\eta = 0.5$. By further comparison of the oil-flow image data from Furman and Breitsamter [30-11] with the computed skin friction lines, it is apparent that the primary vortex separation onset is predicted computationally only \Delta $x/c_r \approx 0.05$ downstream of the experimental data. This good agreement is probably only due to the difference in freestream Mach number between 0.2 (CFD) and 0.14 (exp.) The higher Mach number for the computational case leads to an upstream shift of the primary vortex separation, and thus to a better agreement with the lower-Mach number experiments.

The inner vortical structure is not captured correctly, both in terms of the onset and of the downstream development. The first discrepancy can possibly be attributed to the assumption of fully turbulent flow in the computations and the second discrepancy to the dissipative effects on vortical structures of the chosen turbulence model.

The problematic of laminar-turbulent transition can be alleviated by computing at higher Reynolds numbers, where transition should take place earlier and thus the fully-turbulent assumption is more accurate. A better correlation to experimental data at higher Reynolds numbers was shown by Crippa and Rizzi [30-4] and presented in the previous sections. This is especially true for higher incidences, whereas at the lowest incidence of 13.3°, the computations still showed major discrepancies. The use of rotational (or curvature) corrections to the basic turbulence model does not show substantial improvements in the vortex strength prediction, which further indicates that the computational methods fail to predict the formation stage of the inner vortex, not its development.

To assess the importance of viscous effects, these can be numerically excluded by solving the Euler equations. With a proper choice of grid resolution and numerical dissipation, leading-edge separation can be achieved

even on the blunt geometry. Numerical simulations on this geometry using the Euler equations were last performed and published in the context of the International Vortex Flow Experiment on Euler Code Validation [30-8] (VFE-1). The main interest was then to study the application of Euler solvers also for the blunt leading-edge geometry, given appropriate corrections.

It is now intriguing to notice that the computations performed within this study, show evidence of the inner vortical structure upstream of primary leading-edge separation as already shown in the Section 30.4.3.2.2. Due to the very late primary leading-edge separation attainable in this case it is easier to analyze the flow structure between the apex and primary separation onset, where the inner vortex develops. The inviscid case shows a similar flow topology as all other viscous cases with a thin vortical structure starting in the apex region, which then concentrates outboard near the primary leading-edge vortex and looses strength (Figure 30-32 and Figure 30-33).

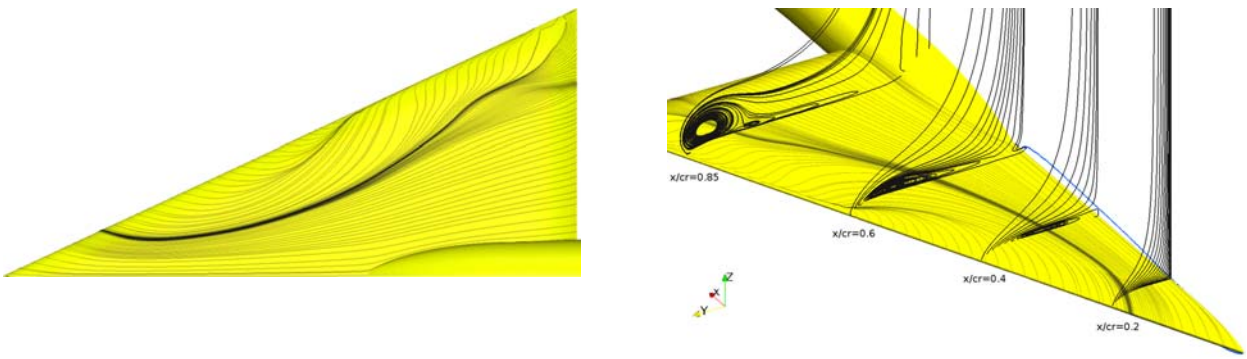

(a) Top View of Suction Side **(b) Isometric View with Field Lines of Force Projected on x/c_r Planes and Attachment Line on Symmetry Plane**

Figure 30-32: Inviscid Case – Skin Friction Lines.

In a plane upstream of the formation of the inner vortex (at $x/c_r \approx 0.1$), the field trajectories reveal fully-attached flow, see Figure 30-33 (a). Between inner vortex formation and primary vortex separation onset (at $x/c_r \approx 0.6$) the inner vortex is comparable in semi-span extent and thickness to the other viscous cases. Since the primary separation is stronger in the inviscid case, the inner vortex is absorbed faster, which results in a different picture at $x/c_r = 0.85$ than for the viscous cases.

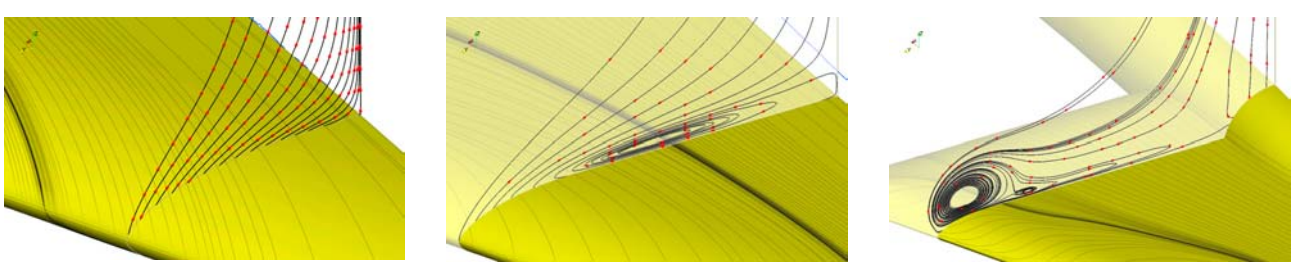

(a) $x/c_r = 0.15$ **(b) $x/c_r = 0.4$** **(c) $x/c_r = 0.85$**

Figure 30-33: Inviscid Case – Isometric Views of Skin Friction Lines and Field Lines of Force Projected on x/c_r Planes.

30.4.3.2.6 Conclusions

Summarizing the results from all cases, the wide, thin inner vortex observed to form very early in the apex region is easily found to attach on the symmetry plane. This may not be true for the experiments, where by comparing with available PIV data it is possible to deduce that the inner vortex is not only located further outboard, but is also stronger and more compact than in the numerical results. If the correct strength and location would be captured correctly by the computations, this could potentially result in the attachment line being shifted from the symmetry plane onto the wing, as shown by the low-speed, low-Reynolds number experiments.

Since the computations under-predict the strength of the inner vortex at its origin, the remaining development can't be matched either. This is consistent with the detailed analysis of the skin friction lines from the computations, where it is not possible to find a distinct convergence of skin friction lines that leads to the inner vortical flow formation. The only squeeze-off type of separations recognizable from the skin friction line analysis are due to the primary and secondary leading-edge vortices. As described by Délery [30-5], this is a common problem also for experimentally obtained oil-flow images at low incidences. The ultimate convergence of streamlines to form a visible separation line can occur far downstream of the saddle point of origin, in the computations an evident convergence does not happen for the inner vortex over the entire wing.

The inviscid case shows the potential to cast light from a different angle on the formation of the inner vortex. It has to be stressed here that due to the nature of inviscid vortical flow computations, it is possible to achieve a fully attached flow solution, or on the contrary a separation very near to the apex, depending on the resolution of the delta-wing surface or several numerical parameters. Given the same reference conditions, an inviscid computation can give very different results. This has been analysed and documented in the past years and the superiority of the RANS methods is proven. But nonetheless, through cautious and deliberate adjustment of the numerical parameters (on a given mesh) it is possible to trigger a pre-determined leading-edge separation position that emulates a desired flow structure. This has been done in this study and the results have to be analysed accordingly with caution, taking account of the restrictions.

In contrast to the general difference in primary (and secondary) leading-edge separation between viscous and inviscid computations, the inner vortical structure is predicted with striking similarity. Due to its mere presence also in the inviscid computations, it is possible to assume that the formation of the inner vortex may be independent of any additional viscous process modelled by the RANS equations. It is possible that for resolving this problem time-accurate computations might be necessary, since it is clear that both inviscid and viscous computations show essentially the same level of discrepancy to the experimental data. Similarly complex multi-vortex systems can be attributed by Gursul et al. [30-13] to the unsteady formation of vortical substructures growing from shear layer instabilities. In this case hybrid turbulence models, such as DES would fail to model the relevant flow physics and LES might be necessary. A detailed analysis of the PIV data by Konrath et al. [30-18],[30-19] reveals indeed also in the presented case the appearance of time-dependent sub-vortices upstream of primary separation onset, that after time-averaging form one vortex as presented Figure 30-30 (a).

30.5 TRANSONIC CASES

Several experimental investigations, e.g., by Elsenaar and Hoeijmakers [30-10], have determined that slender delta wings at transonic freestream conditions can experience a substantial motion of the vortex breakdown location due to a minimal variation of the incidence. The abrupt topological flow rearrangement is due to a non-linear shock-vortex interaction. The computational analysis and understanding of this phenomenon has been a major task within AVT-113/VFE-2, involving the combined efforts of several task group members [30-25]. The following sections will address as much as possible the contribution by KTH to this topic, even though some duplication of data is unavoidable for the sake of clarity.

30.5.1 Introduction

At transonic conditions, the occurrence of shock waves on delta wings at moderate to high angles of attack leads inevitably to shock-vortex interactions. For the majority of conditions, the shock waves are weak enough, or are located appropriately, to substantially have little influence on the vortex development. In these conditions a "classical" vortex breakdown is found at the trailing edge of the delta wing. These situation is found in the common VFE-2 cases of the sharp and blunt configuration at $\alpha = 18.5°$, $M = 0.85$, $R_{mac} = 6 \times 10^6$. Good correlation between computational and experimental results is not only found for this condition, but also for higher angles of attack, up to a certain critical value.

30.5.2 Test Case

The same numerical settings and physical modelling is used for the transonic cases as for other RANS computations. In this section, additionally to the RANS results, some unsteady results are presented, which are the results of a DES computation. For the only DES result presented in this section, 10760 time steps are performed with 100 explicit sub-iterations. The outer time step is set to 1.64×10^{-5}s, which corresponds to the non-dimensional value of 0.0048. Time-averaged DES results presented here are the results of averaging between the outer time steps 9550 and 10465.

The basic condition for the assessment of the transonic effects is $\alpha = 23.0°$, $M = 0.85$, $R_{mac} = 6 \times 10^6$ for the sharp leading edge configuration. At this condition, the experimental datasets show vortex breakdown to occur above the trailing edge, but several CFD investigations consistently predict vortex breakdown to occur at a chordwise position of approx. $x/c_r = 0.67$. The vortex breakdown is induced by one or two strong shock waves placed in front of the sting/wing intersection (at $x/c_r \approx 0.635$). For more details on the results of several task members, please refer to Chapter 29 of this report.

30.5.3 Numerical Grids

The numerical grid used for the investigations by KTH is specifically adapted to the main reference conditions. This is achieved by generating a RANS solution on an initial grid, and then by re-meshing it using TRITET and the RANS solution. This approach differs from the previously presented adaptation approach, as it is possible to achieve an improved, case-specific discretization, without increasing the cell count. In the adaptation approach, it is only possible to add cells to the domain. With the re-meshing approach, the original mesh is used as a back-bone to generate a new, partly skewed and refined mesh. One disadvantage of this approach is that it is not possible to re-mesh the surface grid, as it was generated with ANSYS ICEM CFD and the re-meshing procedure is performed with TRITET. Thus the surface discretization is not changed. The initial grid is presented in Figure 30-34, and the re-meshed volume grid for the main case $\alpha = 23.0°$, $M = 0.85$, $R_{mac} = 6 \times 10^6$ is presented in Figure 30-35.

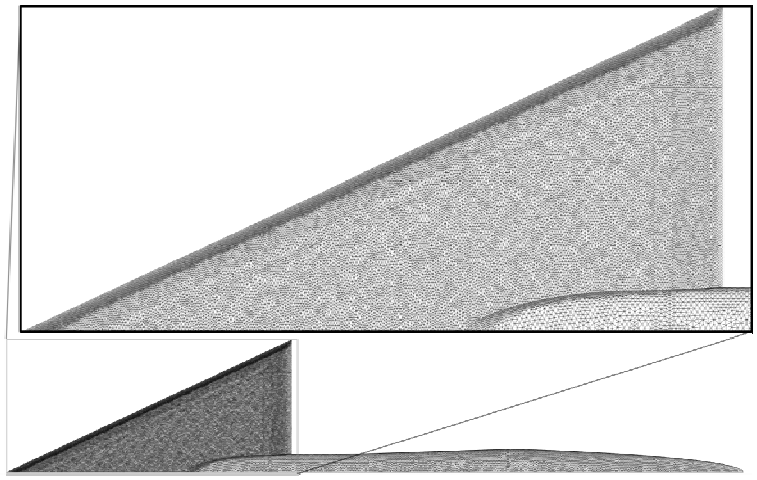

Figure 30-34: Upper Surface of the Initial Numerical Grid of the Sharp Leading Edge Geometry.

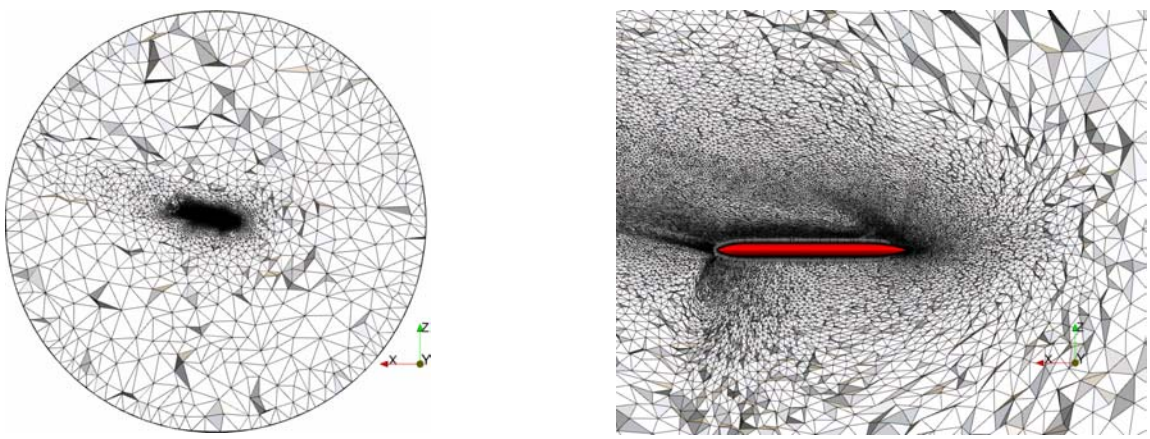

(a) Global Side View **(b) Side View – $x/c_r \approx -0.2 – 1.2$**

Figure 30-35: Re-meshed Grid for Case α = 23.0°, M = 0.85, $R_{mac} = 6 \times 10^6$ – Mid-Span Cut Through Volume (η = 0.5).

Additionally to the sharp leading edge grids described above, two sting-less grids were produced for the sharp and blunt leading edge geometries. The walls of the sting-less grids are discretised exactly as the sting-fitted grids to ease a relative comparison. For a sideslip incidence analysis, the re-meshed grid is mirrored at the symmetry plane. The grid sizes are summarized in Table 30-8 and Table 30-9.

Table 30-8: Computational Grid Size for the Transonic, Sharp Leading Edge Cases – Increase in Comparison to the Initial Grid is Given in Brackets; k = 10^3, M = 10^6 in the Table (Pyramidal elements are included in the total volume nodes counts)

Grid/Case	Total wall surface tri. elements	Prismatic volume cells	Tetrahedral volume cells	Total volume nodes
Initial, with sting	106 k	3.58 M	5.03 M	2.67 M
Remeshed	106 k (**-**)	3.58 M (**-**)	7.19 M (**43%**)	3.02 M (**13%**)
Initial, no sting	101 k	4.05 M	3.55 M	2.67 M
Twice adapted	415 k (**311%**)	16.56 M (**309%**)	22.88 M (**545%**)	12.29 M (**360%**)

Table 30-9: Computational Grid Size for the Transonic, Blunt Leading Edge Cases – Increase in Comparison to the Initial Grid is Given in Brackets; k = 10^3, M = 10^6 in the Table (Pyramidal elements are included in the total volume nodes counts)

Grid/Case	Total wall surface tri. elements	Prismatic volume cells	Tetrahedral volume cells	Total volume nodes
Initial, with sting	169 k	5.25 M	2.36 M	3.09 M
Once adapted	191 k (**13%**)	6.13 M (**17%**)	3.46 M (**47%**)	3.73 M (**21%**)
Initial, no sting	137 k	4.39 M	2.37 M	2.64 M
Twice adapted	148 k (**8%**)	4.74 M (**8%**)	4.50 M (**90%**)	3.18 M (**20%**)

30.5.4 Comparison of Numerical Grids

Here we present the comparison in terms of relative solution accuracy between the initial grid and the re-meshed grid for the sharp configuration. A field cut-plane through the vortex core reveals in Figure 30-36 the improved resolution of flow details given by the re-meshed grid. Furthermore, the vortex core axial velocity and pressure ratio are presented in Figure 30-37. Here it is possible to recognize that the re-meshed grid, which is based on a RANS solution, shows the same solution accuracy also for another position of the shock/vortex interaction zone. The re-meshed grid was used also for the unsteady analysis.

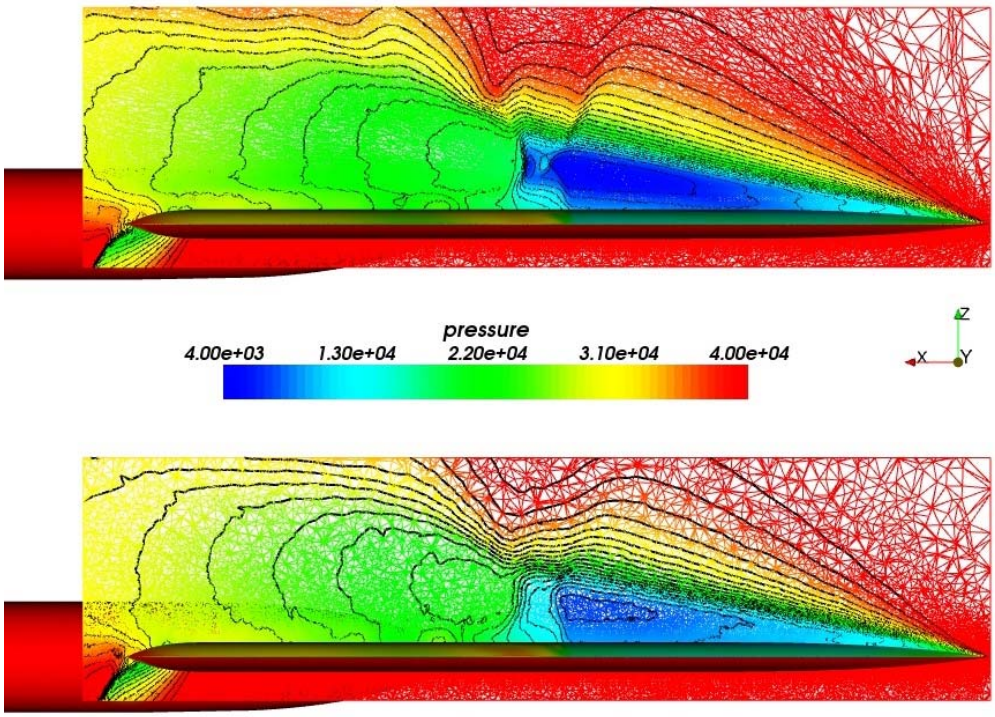

Figure 30-36: Constrained Volume Cut of the RANS Solution for Case α = 23.0°, M = 0.85, R_{mac} = 6 x 10^6 – Upper Sub-Frame: Re-meshed Grid, Lower Sub-Frame: Initial Grid.

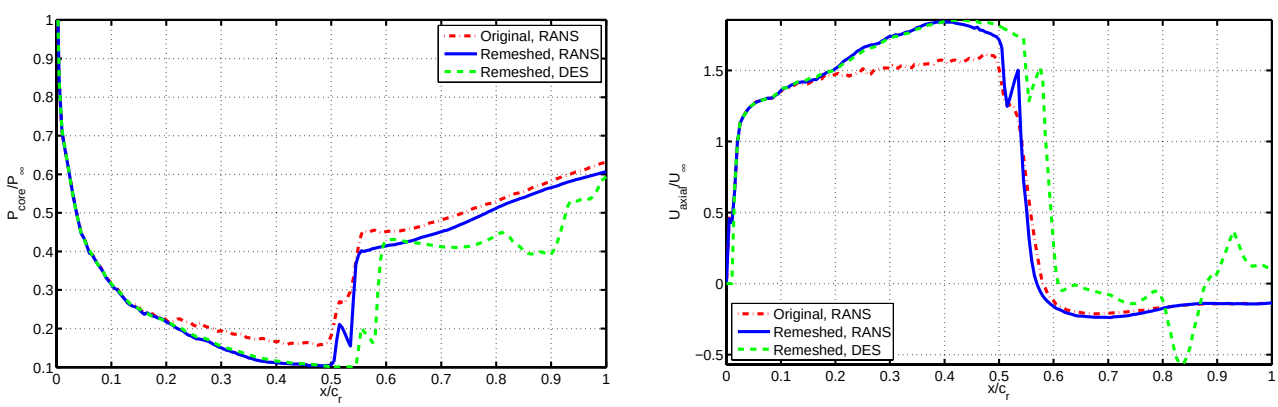

(a) Normalized Static Pressure in the Vortex Core **(b) Normalized Vortex Core Axial Velocity**

Figure 30-37: Comparison between Re-meshed Grid and Initial Grid for Case α = 23.0°, M = 0.85, R_{mac} = 6 x 10^6 – "DES" refers to the solution at a single time step.

30.5.5 Results

As previously described, this section is mainly focussed on presenting the contribution of KTH to the common task of understanding the sudden motion of the breakdown location. Possible factors of influence on the

discrepancy between computations and experiments are presented hereafter. A full discussion and analysis of this condition is presented in Chapter 29 of this report.

30.5.5.1 Sting Installation

It has been suggested within this task group and e.g. by Schiavetta et al. [30-26] that the shock upstream of the sting is caused by the installation of the sting onto the upper surface of the delta wing. This is in line with common knowledge, but the result of the following study reveals that the sting/wing intersection is not necessary the only reason for the occurrence of a mid-chord shock wave.

The RANS solutions for four different configurations at exactly the same conditions are presented here; sharp and blunt leading edge configuration, each with a sting-fitted and sting-less variant. The upper surface pressure coefficient plots are presented in Figure 30-38. Clearly in the case of the sharp leading edge geometry (Figure 30-38 (a)), the removal of the sting results only in a small difference in the location of the shock wave. The effect on the primary and secondary vortices is very similar. On the other hand, the removal of the sting on the blunt leading edge configuration (Figure 30-38 (b)) reveals a completely different picture. The shock wave is still present, but located approx. at $x/c_r = 0.72$, i.e. 20% of c_r further downstream than in presence of the sting. Since the shock wave is not only located further downstream, but it also is relatively weak, the vortex core can remain coherent up to approx. at $x/c_r = 0.72$. The conjectured cross-flow shock wave, outboard of the suction peak of the vortex core after $x/c_r = 0.72$ seems to join the trailing edge shock wave. The flow features and thus the surface pressure coefficient show a pattern which is very similar to the transonic, sharp leading edge experiments at this angle of attack. By considering the left-hand side of the Figure 30-38 (a) and Figure 30-38 (b), i.e. the difference being only the leading edge (sharp versus blunt), it is remarkable that the location, strength and effect on the vortex core are nearly identical.

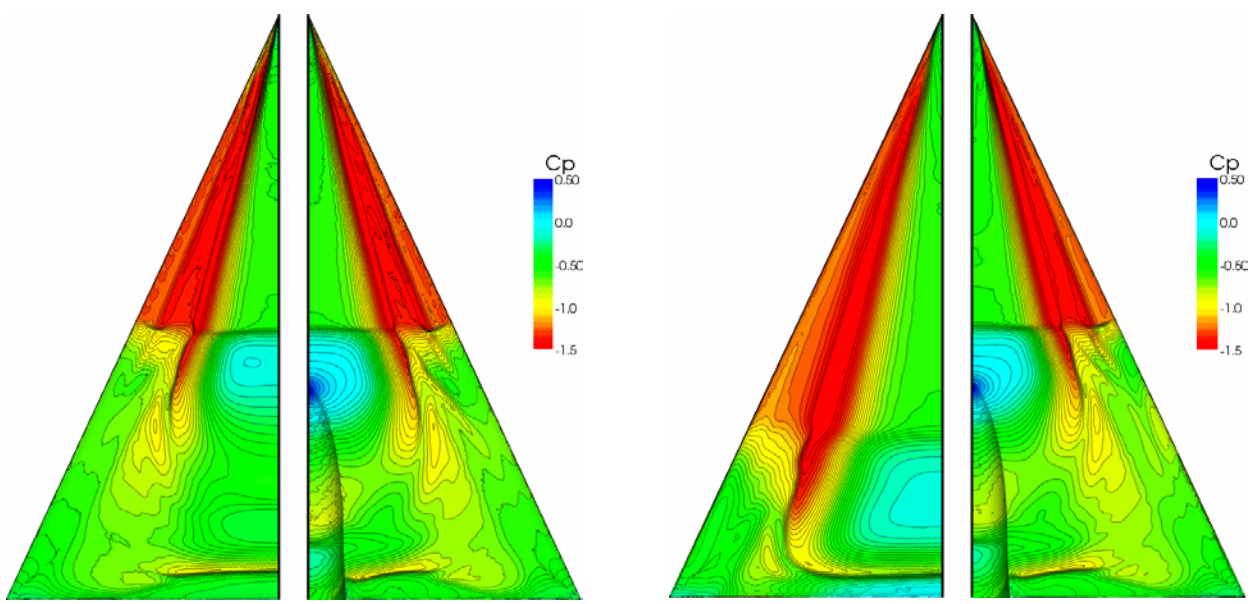

(a) Sharp Leading Edge; Left Sub-Frame: Without Sting, Right Sub-Frame: With Sting

(b) Blunt Leading Edge; Left Sub-Frame: Without Sting, Right Sub-Frame: With Sting

Figure 30-38: Comparison between Sting-Less and Sting-Fitted Solution for the Sharp and Blunt Geometries – RANS Solutions for Case $\alpha = 23.0°$, $M = 0.85$, $R_{mac} = 6 \times 10^6$.

To better study the difference between the four cases it is possible to derive from the CFD solution the Rossby number (Ro) by using a section-wise integration method by Robinson et al. [30-24]. The Rossby number can be used as a metric to determine the vortex intensity or strength. The Rossby number is computed as the ratio of the axial and circumferential momentum of a vortex. For further details on how to determine the Rossby number, refer to Robinson et al. [30-24]. A reduction in the Rossby number is equivalent to a weakening of the vortex core. Within a certain range the vortex becomes susceptible to further disturbances; this range is experimentally found by Robinson et al. [30-24] to lie between 0.9 and 1.4. A Rossby number below zero corresponds to flow reversal, but unrecoverable vortex breakdown happens below Ro = 0.9. The Rossby number between the apex and trailing edge of the four cases is presented in Figure 30-39.

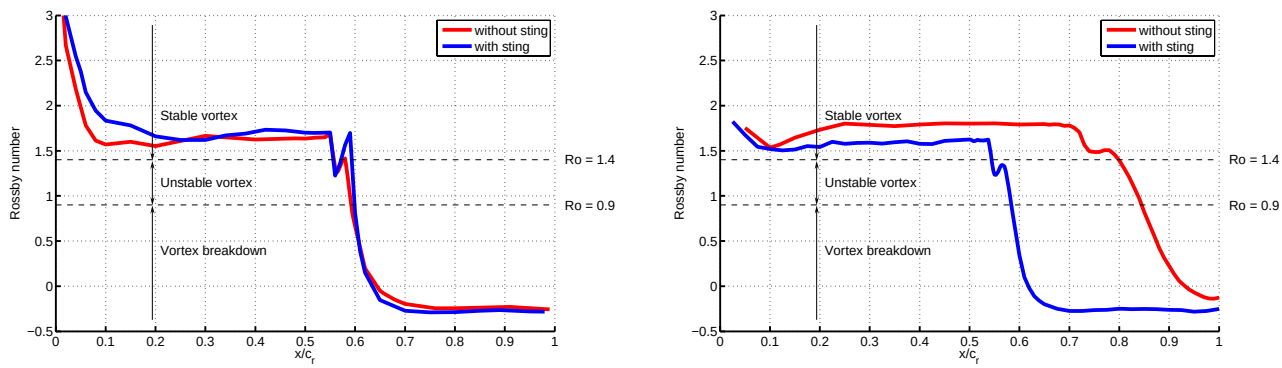

(a) Sharp Leading Edge **(b) Blunt Leading Edge**

Figure 30-39: Rossby Number Comparison between Sting-Less and Sting-Fitted Solution for the Sharp and Blunt Geometries – RANS Solutions for Case α = 23.0°, M = 0.85, R_{mac} = 6 x 10^6.

In case of the sharp leading edge geometry (Figure 30-39 (a)), two local maxima are found around mid-chord. The location of the two peaks is virtually unchanged by the presence of the sting. The first peak corresponds to the first vortex core disturbance by the impinging shock wave, whereas the second peak corresponds to the start of full vortex breakdown. The Rossby number ahead of the first disturbance is similar, and thus also found to be independent of the presence of the sting.

When considering also the Rossby plot of the blunt leading edge geometries (Figure 30-39 (b)), some similarities to the sharp cases appear, but also some striking differences. Two subsequent peaks of Rossby number are found for both blunt leading edge configurations as for both sharp leading edge configurations. In case of the sting-less, blunt leading edge configuration, the Rossby number of upstream of vortex breakdown is markedly higher for the sting-less configuration. The stronger vortex for the blunt, sting-less configuration is able to withstand an abrupt breakdown at x/c_r = 0.72, and only at x/c_r = 0.8 the Rossby number slowly decrease to result in full flow reversal at x/c_r = 0.93. This smooth pattern in the Rossby number plot is only found for the blunt, sting-less configuration at these conditions, but it is very similar to the case α = 18.5°, M = 0.85, R_{mac} = 6 x 10^6 as shown in Chapter 29 and Schiavetta et al. [30-25].

By making a cross-figure comparison between Figure 30-39 (a) and Figure 30-39 (b) for the sting-fitted sharp and blunt configurations, it is possible to identify a similar location of the first disturbance, i.e. the location of the shock wave is similar. The Rossby number upstream of the shock wave is in the same range, thus the similarly strong shock wave reduces the strength of the vortex core by a similar amount. Indeed the lower peak of these two configurations is at Ro = 1.22 for the sharp leading edge case and Ro = 1.24 for the blunt leading edge case.

It has to be noted that Robinson et al. [30-24] derived the values for vortex core stability by using experimental data for subsonic conditions. Thus the breakdown mechanism follows the classical procedure and the Rossby number plots show a distinct, but gradual decrease at vortex breakdown. The presence of two local maxima in the Rossby plots is not documented by Robinson et al. [30-24] and is believed to be a unique feature of a shock-induced vortex breakdown.

30.5.5.2 Sideslip

A possible problem in an experimental campaign is that of a minimal sideslip angle due to unavoidable tolerances in the model support system. This is a possible explanation for the asymmetric PSP data measured by Konrath et al. [30-19]. Numerically it is thus interesting to check for sideslip angle dependency and assess any possible effect on the flowfield.

The pressure coefficient on the symmetry plane is presented in Figure 30-40 (a) for two symmetric ($\beta = 0°$) computations with different physical models, RANS and DES. It is interesting to note that the RANS solution for the symmetric condition agrees perfectly with the time-averaged DES solution in terms of shock location, but not in strength. Three additional results are presented for RANS computations of a full-body configuration at three different sideslip angles, $\beta = 0.1°$, $0.5°$, $1°$. The shock wave ahead of the sting/wing intersection is found to be very sensitive in respect to sideslip angle. An increase of the sideslip angle by a tenth degree results in an upstream movement of the shock wave of approx. $x/c_r = 8\%$. An additional increase to $\beta = 1°$ changes only little in the location of the shock wave. But at this sideslip angle, a new shock wave is present just ahead of the sting/wing intersection. The critical pressure coefficient for the given free-stream conditions is -0.302. The minimum C_p value for the $\beta = 1°$ case is located at $x/c_r \approx 0.6$ and reads -0.466. The upper surface pressure coefficient shown in Figure 30-40 (b) reveals the location and attitude of the two shock waves. With the clear presence of a sting-induced shock wave at $x/c_r \approx 0.6$, the further upstream located shock wave is conjectured not to be caused by the sting, but by a strong flow acceleration in the central part of the wing which is due to the starboard leading edge primary vortex. At a sideslip angle of 0°, these two shock-inducing phenomena combine to induce only one shock wave located in between.

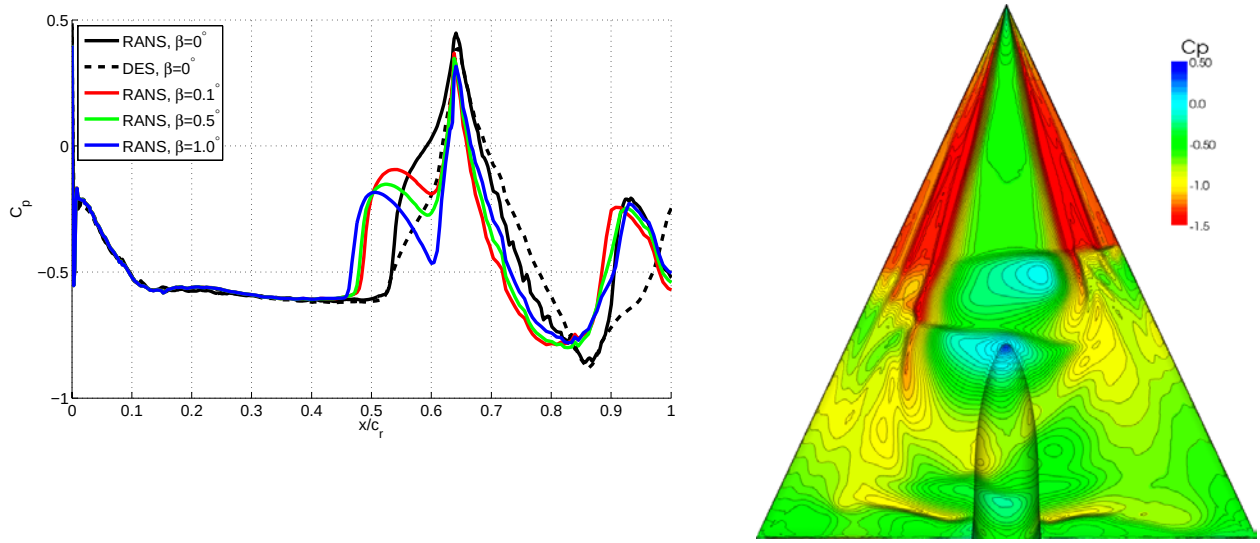

(a) C_p on the Delta Wing and Sting at the Intersection with the Symmetry Plane – "DES" refers to the time-averaged solution

(b) C_p on Suction Side of Delta Wing – RANS Solution of Full-Body, Sharp Leading Edge Geometry at β = 1°

Figure 30-40: Effect of Sideslip Angle on Solution – CFD Solutions for Case α = 23.0°, M = 0.85, R_{mac} = 6 x 10^6 at Various Sideslip Angles (β).

The computations by Glasgow presented in Chapter 29 reveal for the symmetric configuration at the same free-stream condition the presence of two shock waves upstream of the sting/wing intersection. In light of this sideslip analysis it is here suggested that this might be due to the specific turbulence model used for the Glasgow analysis, i.e. the Wilcox k-ω with P_ω enhancer model [30-1]. The modification to the Wilcox k-ω model is specifically targeted to decrease the dissipative nature of the original Wilcox k-ω model. This leads to stronger vortices. If the conjecture described above is correct, then an increase in vortex strength would lead to an increase in mass flow in the central wing section. Thus causing, as in the case of a sideslip angle of 1°, a split-up of the single shock wave seen in this study at β = 0° into two separate.

30.6 REFERENCES

[30-1] Brandsma, J., Kok, J.C., Dol, H.S. and Elsenaar, A.: *Leading Edge Vortex Flow Computations and Comparison with DNW-HST Wind Tunnel Data*, Proceedings of the RTO/AVT Symposium on "Vortex Flows and High Angle of Attack", Loen, Norway, May 2001.

[30-2] Chiba, K., Obayashi, S. and Nakahashi, K.: *CFD Visualization of Second Primary Vortex Structure on a 65-degree Delta Wing*, Proceedings of the 42nd AIAA Aerospace Sciences Meeting and Exhibit, Reno, NV, January 2004, AIAA-2004-1231.

[30-3] Chu, J. and Luckring, J.M.: *Experimental Surface Pressure Data Obtained on 65° Delta Wing Across Reynolds Number and Mach Number Ranges*, Technical Report, NASA TM 4645, NASA Langley Research Center, Hampton, Virginia, 1996.

[30-4] Crippa, S. and Rizzi, A.: *Numerical Investigation of Reynolds Number Effects on a Blunt Leading-Edge Delta Wing*, Proceedings of the 24th Applied Aerodynamics Conference, San Francisco, CA, June 2006, AIAA-2006-3001.

[30-5] Délery, J.M.: *Physics of Vortical Flows*, Journal of Aircraft, 29(5):856-876, September – October 1992.

[30-6] Eberle, A., Rizzi, A. and Hirschel, E.H.: *Numerical Solutions of the Euler Equations for Steady Flow Problems*, Notes on Numerical Fluid Mechanics, Volume 34, Chapter 11, pp. 374-375, Vieweg, 1992.

[30-7] Eliasson, P.: *Edge, a Navier-Stokes Solver for Unstructured Grids*, Proceedings to Finite Volumes for Complex Applications III, pp. 527-534, 2002.

[30-8] Elsenaar, A. and Eriksson, G. editors: *International Vortex Flow Experiment on Euler Code Validation*, FFA, Flygtekniska Försökanstalten, October 1986.

[30-9] Elsenaar, A., Hjemberg, L., Bütefisch, K.-A. and Bannink, W.J.: *The International Vortex Flow Experiment*, Validation of Computational Fluid Dynamics – AGARD-CP-437, Volume 1, pp. 9.1-9.23, AGARD, 1988.

[30-10] Elsenaar, A. and Hoeijmakers, H.W.M.: *An Experimental Study of the Flow Over a Sharp-Edged Delta Wing at Subsonic and Transonic Speeds*, AGARD Conference Proceedings Vortex Flow Aerodynamics, pp. 15.1-15.19, AGARD-CP-494, July 1991.

[30-11] Furman, A. and Breitsamter, C.: *Investigation of Flow Phenomena on Generic Delta Wing*, Proceedings of the 25th International Congress of the Aeronautical Sciences, Hamburg, Germany, 2006, ICAS-2006-3.2.1.

[30-12] Gordnier, R.E.: *Computational Study of a Turbulent Delta-Wing Flowfield Using Two-Equation Turbulence Models*, Proceedings of the 27th AIAA Fluid Dynamics Conference, New Orleans, LA, June 1996.

[30-13] Gursul, I., Gordnier, R.E. and Visbal, M.R.: *Unsteady Aerodynamics of Non-Slender Delta Wings*, Progress in Aerospace Sciences, 41(7):515-557, October 2005.

[30-14] Hellsten, A.: *New Two-Equation Turbulence Model for Aerodynamics Applications*, PhD Thesis, Department of Mechanical Engineering, Helsinki University of Technology (Espoo, Finland), 2004.

[30-15] Hummel, D.: *The Second International Vortex Flow Experiment (VFE-2) – Objectives and First Results*, Proceedings of the 2nd International Symposium on "Integrating CFD and Experiments in Aerodynamics", pp. 1-12, Cranfield University (Shrivenham), UK, 2005.

[30-16] Hummel, D. and Redeker, G.: *A New Vortex Flow Experiment for Computer Code Validation*, Proceedings of the RTO/AVT Symposium on "Vortex Flow and High Angle of Attack Aerodynamics", Loen, Norway, May 2001, 2003.

[30-17] Konrath, R., Klein, C., Engler, R.H. and Otter, D.: *Analysis of PSP Results Obtained for the VFE-2 65° Delta Wing Configuration at Sub- and Transonic Speeds*, 44th AIAA Aerospace Sciences Meeting and Exhibit, 2006.

[30-18] Konrath, R., Schröder, A. and Kompenhans, J.: *Analysis of PIV Results Obtained for the VFE-2 65 Degree Delta Wing Configuration at Sub- and Transonic Speeds*, Proceedings of the 24th Applied Aerodynamics Conference, San Francisco, CA, 2006, AIAA-2006-3003.

[30-19] Konrath, R., Klein, C. and Schröder, A.: *PSP and PIV Investigations on the VFE-2 Configuration in Sub- and Transonic Flow*, Proceedings of the 46th AIAA Aerospace Sciences Meeting and Exhibit, Reno, NV, 2008, AIAA-2008-0379.

[30-20] Lamar, J.E., Cronin, C.K. and Scott, L.E.: *A Review of Steps Taken to Create an International Virtual Laboratory at NASA Langley for Aerodynamic Prediction and Comparison*, Progress in Aerospace Sciences, Volume 40, pp. 163-172, Elsevier Ltd., UK, 2004.

[30-21] Le Moigne, Y.: *Adaptive Mesh Refinement and Simulations of Unsteady Delta-Wing Aerodynamics*, Proceedings of the European Congress on "Computational Methods in Applied Sciences and Engineering", ECCOMAS, 2004.

[30-22] Luckring, J.M.: *Reynolds Number and Leading-Edge Bluntness Effects on a 65° Delta Wing*, Proceedings of the 40th AIAA Aerospace Sciences Meeting and Exhibit. Reno (NV), 2002.

[30-23] Luckring, J.M.: *Reynolds Number, Compressibility and Leading-Edge Bluntness Effects on Delta-Wing Aerodynamics*, Proceedings of the 24th International Congress of Aeronautical Sciences, 2004.

[30-24] Robinson, B.A., Barnett, R.M. and Agrawal, S.: *Simple Numerical Criterion for Vortex Breakdown*, AIAA Journal, Volume 32, No. 1, January 1994, Also presented as Paper 92-0057 at the AIAA 30th Aerospace and Sciences Exhibit.

[30-25] Schiavetta, L.A., Boelens, O.J., Crippa, S., Cummings, R.M., Fritz, W. and Badcock, K.J.: *Shock Effects on Delta Wing Vortex Breakdown*, Proceedings of the 46th AIAA Aerospace Sciences Meeting and Exhibit, Reno, NV, 2008, AIAA-2008-0395.

[30-26] Schiavetta, L.A., Boelens, O.J., Fritz, W. and Cummings, R.M.: *Sting Effects on Transonic Delta Wing Experiments*, Proceedings of the 3rd International Symposium on "Integrating CFD and Experiments in Aerodynamics", U.S. Air Force Academy, CO, USA.

[30-27] Spalart, P., Jou, W.H., Strelets, M. and Allmaras, S.R.: *Comments on the Feasibility of LES for Wings and on a Hybrid RANS/LES Approach*, Proceedings of the 1st AFSOR International Conference on "DNS/LES, Advances in DNS/LES", Greyden Press, 1998.

[30-28] Tysell, L.: *An Advancing Front Grid Generation System for 3D Unstructured Grids*, Proceedings of the 19th Congress of the International Council of the Aeronautical Sciences, ICAS-94-2.5.1, pp. 1552-1564, 1994.

[30-29] Tysell, L., Berglind, T. and Eneroth, P.: *Adaptive Grid Generation for 3D Unstructured Grids*, Proceedings of the 6th International Conference on "Numerical Grid Generation in Computational Field Simulation", pp. 391-400, 1998.

[30-30] Wallin, S. and Johansson, A.V.: *An Explicit and Algebraic Reynolds Stress Model for Incompressible and Compressible Turbulent Flows*, Journal of Fluid Mechanics, 403:89-132, 2000.